Materials Today Nano 31 (2025) 100662

Contents lists available at ScienceDirect

Materials Today Nano

journal homepage: www.sciencedirect.com/journal/materials-today-nano

Deformation mechanisms of AlCoCrCuFeNi: A molecular dynamics and machine learning approach

Hoang-Giang Nguyen [a,b,c], Sheng-Joue Young [b], Thanh-Dung Le [d,e], Symeon Chatzinotas [d], Te-Hua Fang [a,f,*]

[a] Department of Mechanical Engineering, National Kaohsiung University of Science and Technology, Kaohsiung, 807, Taiwan
[b] Department of Electronic Engineering, National United University, Miaoli City, Taiwan
[c] Faculty of Engineering, Kien Giang University, Kien Giang Province, Viet Nam
[d] Interdisciplinary Centre for Security, Reliability, and Trust (SnT), University of Luxembourg, Luxembourg
[e] Department of Electrical Engineering, Écolede Technologie Supérieure, University of Québec, Montréal, Québec, Canada
[f] Department of Fragrance and Cosmetic Science, Kaohsiung Medical University, Kaohsiung, 807, Taiwan

ARTICLE INFO

Keywords:
Mechanical properties
Machine learning
Molecular dynamic
Stress
Dislocation density

ABSTRACT

High-entropy alloys (HEAs) distinguish themselves from other multi-component alloys through their unique nanostructures and mechanical properties. This study employs molecular dynamics (MD) simulations and machine learning to investigate the deformation mechanisms of AlCoCuCrFeNi HEA under varying temperatures, strain rates, and average grain sizes. The modeling results show that interactions between partial dislocations in AlCoCrCuFeNi HEA during tension and compression deformation cause various lattice disorders. The effect of temperature, strain rates, and grain boundaries on lattice disorder, plastic deformation behavior, dislocation density, and von-Mises stress (VMS) is disclosed. This study offers new insights into the atomic-scale deformation mechanisms governing the mechanical behavior of AlCoCrCuFeNi HEAs. It also presents a comprehensive workflow for predicting the mechanical properties of this HEA using machine learning models. The proposed approach provides several advantages, including significantly reduced simulation time and robust model validation. By employing the machine learning model trained in Stage 1, the time needed to simulate mechanical properties in Stage 2 is significantly decreased. Additionally, the framework ensures that the machine learning model effectively captures and understands the underlying representations of the mechanical properties of HEAs, thereby enhancing both the efficiency and accuracy of the predictions.

1. Introduction

The pursuit of materials with superior mechanical properties has continually propelled human technological advancement. Discovering new metals and alloys has been central to this progress. Traditionally, alloys are classified by their dominant elemental component, such as Co-, Cr-, or Ni-based systems [1,2]. High-entropy alloys (HEAs) have emerged as a groundbreaking class of materials, exhibiting properties that transcend conventional multi-component or near-equiatomic alloy concepts. Comprising high concentrations of various elements with distinct crystal structures, HEAs can form stable single-phase solid solutions [3–5]. These multi-element alloys possess elevated configurational entropy in their random solution states, which favors the formation of simple solid solutions rather than complex multiphase microstructures [6,7]. Unlike traditional alloy design focusing on the phase diagram's corners, HEAs offer new pathways to create advanced materials with remarkable potential [8]. At elevated temperatures, atomic diffusion within high-entropy alloys (HEAs) occurs at a sluggish rate, resulting in high activation energy for grain growth and a slower phase transition process [9]. Furthermore, HEAs are often characterized by substantial lattice distortions [10]. These alloys exhibit a range of remarkable properties, including exceptional fracture toughness exceeding that of conventional alloys and pure metals, mechanical strength comparable to metallic glasses and structural ceramics, superconductivity, and notable corrosion resistance [11,12]. The microstructure of materials, such as grain size, twin boundaries, and crystallographic orientation, plays a vital role in determining their mechanical behavior [13,14]. Additionally, the chemical composition of an

* Corresponding author. Department of Mechanical Engineering, National Kaohsiung University of Science and Technology, Kaohsiung, 807, Taiwan.
E-mail address: fang.tehua@msa.hinet.net (T.-H. Fang).

https://doi.org/10.1016/j.mtnano.2025.100662
Received 27 April 2025; Received in revised form 5 July 2025; Accepted 19 July 2025
Available online 22 July 2025

alloy is a key factor influencing its mechanical performance [15]. Therefore, a comprehensive understanding of the interplay between alloy composition, microstructure, and HEA behavior is essential for the advancement of next-generation structural materials. Mechanical properties of materials can be evaluated using various techniques, including cyclic loading [16], tensile testing [17], cutting [18], imprinting [19], scratching [20], and grinding [21]. Among these, indentation tests provide insight into a material's hardness and elastic modulus, enabling the investigation of how intrinsic material characteristics affect deformation under loading [22,23]. During scratching, where the indenter moves laterally across the surface, the mechanical response of the substrate is examined to assess deformation behavior [24,25].

The addition of trace elements to alloy systems has been strategically used to enhance their mechanical performance by improving heat resistance, flexibility, strength, and phase stability [26–28]. The development of multi-element alloy systems represents a novel approach in alloy design, enabling the tailoring of mechanical and chemical properties through compositional control [29–32]. HEAs, typically consisting of five or more principal elements in near-equiatomic proportions, often exhibit properties that are distinct from those of their individual components [33,34]. This compositional complexity has given rise to a new paradigm in alloy design, shifting focus toward the central region of the phase diagram rather than its boundaries [35]. Such an approach addresses fundamental issues in materials science, including phase selection, entropy control, and energy minimization [36,37]. The combination of sluggish diffusion and high mixing entropy in HEAs promotes the formation of stable solid solutions with diverse crystal structures, such as FCC, BCC, and HCP [38–40]. This alloy design strategy has inspired the development of other advanced materials, including bulk metallic glasses and high-entropy ceramics [41–43]. HEAs also demonstrate superior corrosion resistance, thermophysical performance, and magnetic properties, alongside excellent thermal stability and hardness [44–46]. They retain remarkable mechanical properties across a wide temperature range, showing high strength at elevated temperatures and impressive fracture toughness and ductility at cryogenic conditions [47,48]. These characteristics make HEAs promising candidates for applications in cutting tools, radiation-resistant materials, and fracture-resistant components [49,50]. Recent advances highlight how these challenges can be addressed through innovative HEA design. For instance, Chew et al. [51] enhanced the strength and ductility of CoCrFeNiMn HEA using laser-aided additive manufacturing to form hierarchical microstructures. Similarly, Lee et al. [52] employed advanced microscopy and neutron diffraction techniques to elucidate the deformation mechanisms in NbTaTiV and CrMoNbV HEAs. Among HEAs, the equiatomic AlCoCrCuFeNi alloy is particularly noteworthy due to its mechanical strength and structural stability [53]. Its plastic deformation behavior has been extensively studied.

Recent advances highlight the expanding role of machine learning (ML) in accelerating alloy design, particularly in predicting phase stability, microstructure evolution, and thermomechanical behavior. ML-based models have been effectively applied to forecast phase transformations and identify stable structures in complex alloy systems, such as high-entropy alloys (HEAs) and metallic glasses [54,55]. Moreover, studies [56,57] demonstrate the power of ML in exploring compositional design spaces and predicting phase behavior across diverse alloy compositions. These developments reveal ML's potential not only as a predictive tool but also as a means to significantly reduce the experimental and computational costs traditionally associated with alloy development. Building upon this foundation, this study introduces a two-stage MD–ML framework to predict stress and dislocation behavior in AlCoCrCuFeNi HEA, providing a time-efficient, physics-informed approach to understanding its mechanical response. Jiang et al. [58] investigated the mechanical responses of face-centered cubic (FCC) HEAs across a broad range of strain rates and temperatures, revealing transitions in plastic deformation mechanisms under dynamic uniaxial tension. Zhang et al. [59] fabricated single-crystalline CoCrFeNi HEA micropillars with various crystallographic orientations and performed in situ compression tests, elucidating deformation mechanisms at the micro/nanoscale. Similarly, Cao et al. [60] combined mechanical testing and molecular dynamics simulations to explore dynamic deformation in CoCrFeNi HEAs, offering insights for designing alloys with superior dynamic performance.

This study presents a detailed workflow for predicting the mechanical properties of high-entropy alloys, specifically the AlCoCuCrFeNi HEA, using machine learning (ML) models. The workflow is divided into two distinct stages, each comprising three phases: molecular dynamics simulation, ML training, and prediction.

The workflow begins with multiphysics simulations of the AlCoCrCuFeNi HEA in Stage 1. The initial atomic and grain configurations of the HEA nanomaterial are constructed, followed by molecular dynamics (MD) simulations to extract key material parameters, including strain (%), temperature (K), grain size (nm), and strain rate (s^{-1}). These parameters serve as input features for training a neural network model designed to predict the material's stress response (GPa). The resulting predictions offer detailed insight into the material's tensile behavior, illustrated through a visual stress distribution.

In Stage 2, transfer learning is employed to improve model performance. The same HEA undergoes further MD simulations, using the previously learned features from Stage 1. The pre-trained model is fine-tuned with new data to predict dislocation density (nm^{-2}), enabling the exploration of nanoscale deformation mechanisms. This stage culminates in a dislocation density map, providing a comprehensive depiction of the material's internal structural evolution under mechanical loading.

The proposed workflow offers significant benefits, including reduced simulation times and robust model validation. By utilizing the trained ML model from Stage 1, the overall simulation time required for obtaining mechanical properties in Stage 2 is significantly decreased. Moreover, this framework ensures that the ML model effectively captures and learns the hidden representations of mechanical properties in HEA materials, enhancing the efficiency and accuracy of property predictions. This methodological approach demonstrates the successful integration of molecular dynamics simulations with advanced ML techniques to predict and understand the mechanical properties of complex materials like high-entropy alloys.

2. Methodologies and materials

2.1. Molecular simulation

Molecular dynamics is a method employing physical principles to approximate the average properties of an atomic system, governed by classical Newtonian mechanics, computed over time. This model often represents atoms as point masses within a simulated box, resulting in rigid spherical shapes. The interaction between neighboring atoms is regulated by a force field determined by the user, known as the interaction potential. Subsequently, partial charges can be estimated using quantum methods to describe the distribution of charge within molecules. Bonds between atoms are typically depicted as simple harmonic oscillations with constraints on angles. Upon commencement of the simulation, a velocity range corresponding to the Boltzmann distribution at the appropriate temperature is selected, and these velocities are then randomly assigned to each atom. Similar processes are employed to provide energy for bonds and angles. Subsequently, the simulation proceeds using Newtonian physics, wherein molecules transfer motion and energy to one another through atomic interaction forces and electrostatic forces. The molecular mechanics energy function used in MD is a potential energy function that remains time-invariant and depends solely on the spatial coordinates of atoms or molecules. It conserves the overall energy of the system over time. Consequently, the total kinetic energy (KE) and total potential energy (PE) may fluctuate indepen-

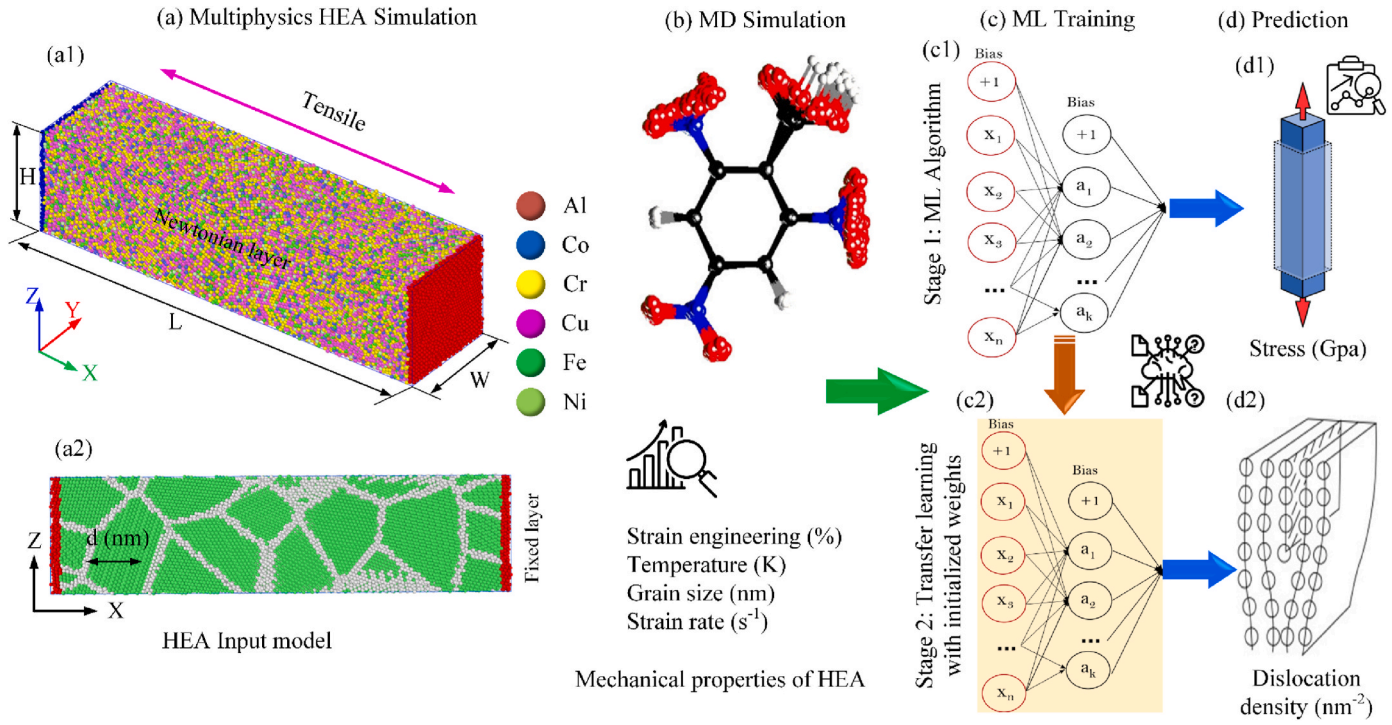

Fig. 1. The graphical abstract illustrates the transfer learning from stress analysis to predict dislocation properties of AlCoCrCuFeNi.

dently. Still, their sum, also called the Hamiltonian (H), always remains a conserved quantity, as demonstrated in equation (1) [61].

$$H = K_e + U_e \tag{1}$$

The kinetic energy (K_e) is defined by the velocity or linear momentum of each individual atom, as indicated in equation (2). Conversely, the potential energy (U_e) is governed by the positional vectors of all atoms, as illustrated in equation (3.3).

$$K_e = \frac{1}{2}\sum_{j=1}^{n} m_i v_i^2 \tag{2}$$

$$U_e = \sum_{i=1}^{n} P_i(u) \tag{3}$$

In a system comprising N atoms, the variables m_i, v_i, P_i, and u_i represent the mass, velocity, potential energy, and position, respectively, of the ith atom.

Molecular dynamics simulations involve the iterative computation of classical equations of motion, particularly evident in a basic atomic system, as outlined below [62–64]:

$$F_i = m_i \ddot{r_i} = m_i a_i = -\frac{\partial}{\partial r_i} u \tag{4}$$

$$m_i \frac{d^2 p_i}{dt^2} = -\frac{dU(p)}{dp_i} \tag{5}$$

Here, m_i and a_i denote the mass and acceleration of the ith atom, respectively. The U(p) signifies the potential energy associated with the interaction. In this segment, it's imperative to compute the forces, denoted as F_i, exerted on atoms, typically stemming from the potential energy function $U(r^N)$. Here, $r^N = (r_1, r_2, \ldots, r_N)$ denotes the entire set of integer coordinates from 3N.

In the context of this research, we employed the simulation platform introduced by Plimpton et al. [65,66], which entails a large-scale atomic/molecular massively parallel simulator known as LAMMPS, to conduct evaluations of the mechanical properties of AlCoCrCuFeNi HEA. LAMMPS, implemented in C++, represents a highly portable classical Molecular Dynamics (MD) code. This platform facilitates the simulation of particle behavior across various length and time scales. Additionally, LAMMPS can execute calculations on parallel machines featuring many processors while maintaining performance levels and avoiding undue increments in system size and complexity. Numerous variations of the Verlet algorithm exist, each essentially equivalent, such as the original method [67,68] and the 'leapfrog' form [69]. Our attention is directed toward the velocity-Verlet algorithm [70].

$$p_i\left(t+\frac{1}{2}\delta t\right) = p_i(t) + \frac{1}{2}\delta t f_i(t) \tag{6}$$

$$r_i\left(t+\frac{1}{2}\delta t\right) = r_i(t) + \frac{\delta t p_i\left(t+\frac{1}{2}\delta t\right)}{m_i} \tag{7}$$

$$r_i\left(t+\frac{1}{2}\delta t\right) = r_i(t) + \frac{\delta t p_i\left(t+\frac{1}{2}\delta t\right)}{m_i} \tag{8}$$

By equation (7), the process of force evaluation is executed to yield f_i $(t + \delta t)$ for step (8). This approach facilitates the progression of coordinates and moments by the time increment δt.

An ensemble refers to a set of distinct states of a given system, with NVE, NPT, and NVT being fundamental examples. Each ensemble serves a specific purpose, where E, N, V, P, and T denote the total energy, number of atoms, volume, pressure, and temperature, respectively. The NVE ensemble, often termed the microcanonical ensemble, maintains fixed N, V, and E, permitting only the velocities and positions of atoms to vary, thus enabling the calculation of macroscopic properties such as changes in kinetic energy, temperature, and pressure. In contrast, the NVT ensemble, known as the canonical ensemble, keeps N, V, and T constant, allowing energy and pressure to fluctuate over time. The NPT ensemble, or isothermal-isobaric ensemble, facilitates rapid structural equilibrium by permitting volume adjustments in response to energy changes [71].

As shown in Fig. 1(a), the AlCoCrCuFeNi high-entropy alloy (HEA)

specimen was subjected to uniaxial tensile loading to investigate its plastic deformation mechanisms and mechanical behavior. The simulation model measures 300 × 75 × 75 Å^3 (length × width × height) and contains approximately 146,117 to 146,315 atoms. The atoms are randomly distributed in a three-dimensional face-centered cubic (FCC) lattice, with coordinates spanning the x, y, and z directions. The sample is oriented along the [100], [010], and [001] crystallographic directions corresponding to the X-, Y-, and Z-axes, respectively. The alloy composition is approximately 9 % Co, 2 % Al, 32 % Cr, 12 % Fe, 39 % Cu, and 6 % Ni [17]. Strain was applied uniaxially along the [100] direction at strain rates ranging from 10^8 to 2 × 10^{10} s^{-1}. Temperature conditions varied from 300 K to 1000 K. The embedded-atom method (EAM) potential, augmented with a Morse term, was used to describe interatomic interactions. Periodic boundary conditions were applied in all directions. Grain sizes from 6.42 to 12.84 nm were generated and characterized using standard Voronoi tessellation. Atomic configurations were analyzed for dislocation content, phase transformation, and local von Mises stress.

In preparing the specimens for tensile stress, all three orientations were subjected to periodic boundary conditions to achieve stable configurations. Employing the conjugate gradient algorithm, samples were generated with minimized equilibrium energy. Subsequently, the samples underwent thermodynamic equilibration for 100 ps at ambient temperature and zero pressure, facilitated by the isothermal-isobaric (NPT) ensemble [16,72]. Integration of the motion equation was achieved using the velocity-Verlet approach, utilizing a time step of 2 fs [73,74]. Pressure and temperature regulation during the tension process was facilitated by the Nosé-Hoover thermostat and barostat, as implemented in this investigation [75–78]. Selecting a dependable potential measure between atoms is paramount in ensuring the accuracy of findings in molecular dynamics (MD) simulations. Thus, to delineate and scrutinize interatomic interactions between Ni, Co, Cu, Cr, Fe, and Al, the Embedded-Atom-Method (EAM) was employed.

The effectiveness of Embedded Atom Method (EAM) potentials has been validated through various prior studies employing diverse testing methodologies [27]. The total energy E_{pt} is expressed in Refs. [23,79].

$$E_{pt} = \sum_{i=1}^{n} E_i = \frac{1}{2} \sum_{\substack{i,j=1 \\ i \neq j}}^{n} \varphi_{ij}(r_{ij}) + \sum_{i=1}^{n} F_i(\rho_i) \tag{9}$$

The pair energy φ_{ij} represents the interaction energy between atoms *i and j as a function of their separation, while* E_i denotes the atomic potential energy of atom *i*. The embedding energy term, defined by r_{ij} and $F_i(\rho_i)$, depends on the local electron density ρ_i, at each atom. The local electron density ρ_i, determined using:

$$\rho_i = \sum_{\substack{i,j=1 \\ i \neq j}}^{n} f_{ij}(r_{ij}) \tag{10}$$

Here, $f_{ij}(r_{ij})$ represents the electron density contribution from atom *j* to the position of particle *i*. The EAM alloy potential model specifies the pair potentials as follows:

$$\phi(r) = \frac{A \exp\left[-\alpha\left(\frac{r}{r_e}\right) - 1\right]}{1 + \left(\frac{r}{r_e} - \kappa\right)^{20}} - \frac{B \exp\left[-\beta\left(\frac{r}{r_e}\right) - 1\right]}{1 + \left(\frac{r}{r_e} - \lambda\right)^{20}} \tag{11}$$

The cutoff parameters for the electron density function are represented by κ and λ, alongside adjustable parameters A, B, α, and β. The equilibration separation between nearest neighbors is symbolized by r_e. The calculation of the electron density function mirrors the form of the attractive term in the pair potential, maintaining identical values for β and λ [79]. The electron density is formulated as:

$$f(r) = \frac{f_e \exp\left[-\beta\left(\frac{r}{r_e} - 1\right)\right]}{1 + \left(\frac{r}{r_e} - \lambda\right)^{20}} \tag{12}$$

Subsequently, a pair potential is defined for two distinct species, denoted as *a* and *b*, as follows:

$$\phi^{nm}(r) = \frac{1}{2}\left[\frac{f^m(r)}{f^n(r)}\phi^{nn}(r) + \frac{f^n(r)}{f^m(r)}\phi^{mm}(r)\right] \tag{13}$$

The following formulas [79] specify the embedding energy functions across various electron density ranges.

$$F(\rho) = \sum_{i=0}^{3} F_{ni}\left(\frac{\rho}{0.85\rho_e} - 1\right)^i, \rho < 0.85\rho_e \tag{14}$$

$$F(\rho) = \sum_{i=0}^{3} F_i\left(\frac{\rho}{\rho_e} - 1\right)^i, 0.85\rho_e \le \rho < 1.15\rho_e \tag{15}$$

$$F(\rho) = \sum_{i=0}^{3} F_n\left[1 - \eta \ln\left(\frac{\rho}{\rho_s}\right)\right]\left(\frac{\rho}{\rho_s}\right)^{\eta}, \rho \ge 1.15\rho_e \tag{16}$$

Here, F_{ni}, F_i, and F_n represent tabulated constants [77,80].

The Morse potential, which dictates the remaining particle interactions [22], is expressed as follows:

$$\Phi(u_{ij}) = D\left[e^{-2\alpha(u_{ij}-u_0)} - 2e^{-\alpha(u_{ij}-u_0)}\right] \tag{17}$$

In the interatomic potential model, the reciprocal energy and distance constants are represented by D and α, respectively. The equilibrium and instantaneous separations between two approaching atoms are represented by u_0 and u_{ij}, respectively. The determination of the average grain size, represented as *d*, is based on methodologies outlined in [81–83]:

$$d = \sqrt[3]{\frac{6V}{N}} \tag{18}$$

Where V denotes the polycrystalline's overall volume of AlCoCrCuFeNi HEA, and N denotes the number of grains. The investigation employs eight workpieces characterized by average grain sizes ranging from 12.84 nm to 6.42 nm, with corresponding grain counts of samples 5, 10, 15, 20, 25, 30, 35, and 40.

This section utilizes analytical techniques to investigate the

Table 1
Statistical exploratory data analysis for stress values prediction dataset (Stage 1).

	Strain	Temperature (K)	Grain number	Strain rate (s^{-1})	Stress (Gpa)
Count	22021	22021	22021	22021	22021
Mean	9.9997 × 10^{-2}	427.2785	29.09913	2.400064 × 10^9	3.345523
Std	5.7791 × 10^{-2}	217.8109	7.012762	4.356896 × 10^9	0.901617
Min	0	300	5.0	1.000000 × 10^8	−0.017224
25 %	5.0000 × 10^{-2}	300	20.0	1.000000 × 10^9	3.961448
50 %	1.0000 × 10^{-1}	300	20.0	1.000000 × 10^9	3.592606
75 %	1.5000 × 10^{-1}	500	20.0	2.000000 × 10^9	3.807873
Max	2.0000 × 10^{-1}	1000	40.0	2.000000 × 10^{10}	5.746938

Table 2
Statistical exploratory data analysis for dislocation density values prediction dataset (Stage 2).

	Strain	Temperature (K)	Grain number	Strain rate (s^{-1})	Dislocation density (nm^{-2})
Count	4400	4400	4400	4400	4400
Mean	0.1005226	427.3017	8.226849	2.400318×10^{9}	0.19924
Std	0.05777293	217.8438	1.230335	4.357648×10^{9}	0.072885
Min	0.001	300	6.42	1×10^{8}	0.05984
25 %	0.051	300	8.09	1×10^{9}	0.15005
50 %	0.101	300	8.09	1×10^{9}	0.18587
75 %	0.151	500	8.09	1×10^{9}	0.23523
Max	0.200	1000	12.84	2×10^{10}	0.5312

deformation mechanism and structural transformations. The progression of deformation during the tension process is illustrated through the von-Mises shear strain [84]. The crystal structure, including stacking defects and phase transitions, is analyzed using Honeycutt and Andersen's common neighbor analysis [85]. Dislocation evolution during the stress process is examined through dislocation extraction analysis (DXA) [86].

2.2. Machine learning

2.2.1. Data

To obtain the data for training and predicting stress values, we conducted Molecular Dynamics (MD) simulations for 118 days using a system equipped with the following specifications: i) Processor: Intel(R) Core (TM) i7-10700 CPU @ 2.90 GHz (16 CPUs), 2.9 GHz, and ii) Memory: 16 GB RAM. Then, for each temperature range (200 K, 300 K, etc.), we defined a step size for strain as 0.0002 (ranging from 0 to 0.2), resulting in 1000 steps. This detailed and high-resolution data collection is crucial for capturing the intricate dependencies between input features and stress values.

Table 1 provides a comprehensive statistical exploratory data analysis of the dataset used for stress values prediction in Stage 1. The table includes critical features such as strain, temperature, grain number, strain rate, and the resulting stress values. The data consists of 22,021 samples, providing a robust basis for training the machine learning model to predict stress in the AlCoCrCuFeNi HEA material.

In Stage 2, we applied transfer learning to enhance predictions further. This stage involves MD simulations with a larger step size of 0.001 for strain (ranging from 0 to 0.2), resulting in a total MD simulation time of 29 days, significantly shorter than the first stage. The same input features are used, focusing on predicting dislocation densities. This reduction in step size by a factor of five allows for quicker yet accurate data collection.

Table 2 provides a statistical exploratory data analysis for the dislocation values prediction dataset in Stage 2. This table includes strain, grain size, temperature, strain rate, and the resulting dislocation values. The dataset consists of 4400 samples, providing a solid foundation for training the refined ML model to predict dislocation densities in the HEA material.

By utilizing the trained ML model from Stage 1, the overall simulation time required for obtaining mechanical properties in Stage 2 is significantly decreased. This framework ensures that the ML model effectively captures and learns the hidden representations of mechanical properties in HEA materials, enhancing the efficiency and accuracy of property predictions. This methodological approach demonstrates the successful integration of multiphysics simulations with advanced ML techniques to predict and understand the mechanical characteristics of complex materials like high-entropy alloys.

2.2.2. Data experimental setup

Our study was conducted on high-performance GPUs available through Google Colab's cloud service. Model implementation utilized the scikit-learn library and the Keras framework in a Python environment. For each experiment, the dataset was split into 70 % for training and 30 % for evaluation to assess model performance.

Building on previous research in neural network optimization, we employed strategies to enhance our model's performance and stability. This approach incorporated dropout with a probability of 0.25 to mitigate overfitting by omitting random units during training. We selected the GlorotNormal initializer to maintain proportional variance between output and input, optimizing weight initialization. Additionally, batch normalization was applied to accelerate training and improve performance by normalizing layer inputs. These hyperparameters were meticulously selected and fine-tuned to maximize model performance.

2.2.3. Machine learning predictive models

Machine learning (ML) enhances the analysis of large datasets by developing trained models that support tasks such as classifying observations, detecting critical features influencing performance metrics, and forecasting outcomes in new experiments. Furthermore, ML aids researchers in data-intensive disciplines by optimizing experimental design to improve performance or streamline hypothesis testing. ML transforms data collection, analysis, and interpretation across diverse domains, including nano-optoelectronics, catalysis, and bio-nano interfaces. These approaches are anticipated to become discipline-specific benchmarks, reinforcing the importance of statistical methods in scientific inquiry. Additionally, nanoscience has the potential to advance ML by developing electronic or photonic hardware that enables more efficient algorithm execution compared to conventional computing architectures. Fostering this synergy promises significant advantages for both scientific communities.

This study will apply ML techniques to predict stress values from MD simulation data. The application of ML in materials science has grown due to its advantages. For instance, conducting real experiments with superconducting materials is very costly and challenging [87]. In particular, deep learning proves to be more advanced and robust for material applications [88]. The study will focus on various ML techniques for regression models, ranging from conventional methods to deep learning models. The performance of each model will be assessed by comparing evaluation metrics, model complexity, and computational resource requirements, including.

1. Linear Regression (LR): Linear Regression [89] presupposes a linear relationship between input features $x = (x_1, x_2, x_3, x_4)$ and the output y. The model estimates y through the linear function:

$$y = \beta_0 + \beta_1 x_1 + \beta_2 x_2 + \beta_3 x_3 + \beta_4 x_4 + \varepsilon \quad (19)$$

Here, β_0 represents the intercept, β_1, …, β_4 denotes the coefficients, and ε signifies the error term.

2. Support Vector Regression (SVR): SVR [90] seeks to identify a function $f(x)$ that deviates from y by at most ε for each training point while maintaining maximal flatness. Mathematically:

$$f(x) = w \cdot x + b \quad (20)$$

Here, w represents the weight vector, and b denotes the bias. Flatness is ensured by minimizing $|w|$, subject to the constraint $|y_i - f(x_i)| \leq \varepsilon$, or

by incorporating slack variables ξ_i or ξ^*_i when required.

3. Gradient Boosting Regression (GBR): GBR [91] constructs a sequential model by minimizing a differentiable loss function. In each iteration, a regression tree $h_m(x)$ is trained to approximate the negative gradient of the loss function $L(y, F(x))$:

$$F_m(x) = F_{m-1}(x) + \gamma_m h_m(x) \tag{21}$$

Here $F_m(x)$ represents the model at the m-th iteration, while γ_m denotes the step size.

4. Feedforward Neural Network (FFNN): An FFNN is a feedforward artificial neural network comprising at least three layers-input, hidden, and output-where each node (excluding the input layer) employs a nonlinear activation function. The output y is expressed as:

$$y = f(W_2 f(W_1 x + b_1) + b_2) \tag{22}$$

Here W_1 and W_2 represent the weights, b_1 and b_2 denote the biases, and f is the activation function. Deep learning models [92] such as Convolutional Neural Networks (CNNs), Long Short-Term Memory (LSTM), Bidirectional Long Short-Term Memory (BiLSTM), Gated Recurrent Unit (GRU), and Recurrent Neural Network (RNN) networks will also be explored.

5. Convolutional Neural Network (CNN): While predominantly applied to image data, CNNs [93] are also effective for sequential data. The convolutional layers detect local dependencies, and the fully connected layers generate the output prediction. For a configuration with a single convolutional layer followed by a fully connected layer:

$$y = W_f \cdot (flatten(R_eLU(W_c * x + b_c))) + b_f \tag{23}$$

where * denotes convolution, W_c and b_c are convolutional layer parameters, and W_f and b_f are fully connected layer parameters.

6. Long Short-Term Memory (LSTM): An LSTM [94] is a variant of a recurrent neural network (RNN) designed to capture order dependencies in sequence prediction tasks. For a single LSTM cell, the output k_t at time t is given by:

$$k_t = o_t \odot \tanh(c_t) \tag{24}$$

Here o_t represents the output gate, c_t denotes the cell state, and $\odot$ indicates element-wise multiplication. The cell state is updated through gates that regulate the flow of information:

$$k_t = o_t \odot \tanh(c_t) \tag{25}$$

Here, o_t represents the output gate, c_t denotes the cell state, and $\odot$ indicates element-wise multiplication. The cell state is modified via a sequence of gates that regulate information flow:

$$f_t = \sigma(W_f \cdot [k_{t-1}, x_t] + b_f) \tag{26}$$

$$i_t = \sigma(W_i \cdot [k_{t-1}, x_t] + b_i) \tag{27}$$

$$\tilde{c}_t = \tanh(W_c \cdot [k_{t-1}, x_t] + b_c) \tag{28}$$

$$c_t = f_t \odot c_{t-1} + i_t \odot \tilde{c}_t \tag{29}$$

$$o_t = \sigma(W_o \cdot [k_{t-1}, x_t] + b_o) \tag{30}$$

In this context, f_t is the forget gate, i_t denotes the input gate, $\tilde{c}_t$ is the candidate cell state, σ indicates the sigmoid function, and W and b are the weights and biases associated with each gate.

7. Bidirectional Long Short-Term Memory (BiLSTM): BiLSTM [95] extends the LSTM framework, enhancing model performance by processing data in both forward and backward directions. For a given sequence, the forward $\overrightarrow{k_t}$ and backward $\overleftarrow{k_t}$ hidden states are concatenated to form the final output:

$$\overrightarrow{k_t} = \left[\overrightarrow{k_t}, \overleftarrow{k_t}\right] \tag{31}$$

where $\overrightarrow{k_t}$ is computed from start to end, and $\overleftarrow{k_t}$ from end to start.

8. Gated Recurrent Unit (GRU): GRU [96] is a type of RNN that simplifies the LSTM architecture by combining the forget and input gates into a single update gate. The hidden state ht at time t is calculated as:

$$k_t = (1 - z_t) \odot k_{t-1} + z_t \odot \tilde{k}_t \tag{32}$$

Where z_t is the update gate and $\tilde{k}_t$ is the candidate hidden state. The update gate z_t and reset gate r_t are defined as:

$$z_t = \sigma(W_z \cdot [k_{t-1}, x_t] + b_z) \tag{33}$$

$$r_t = \sigma(W_r \cdot [k_{t-1}, x_t] + b_r) \tag{34}$$

$$\tilde{k}_t = \tanh(W \cdot [r_t \odot k_{t-1}, x_t] + b) \tag{35}$$

9. Recurrent Neural Network (RNN): RNN [97] is a type of neural network designed for sequence data. The model retains a hidden state h_t that encapsulates information from prior time steps. The hidden state and output y_t at time t are expressed as:

$$k_t = \tanh(W_k \cdot [k_{t-1}, x_t] + b_k) \tag{36}$$

$$y_t = W_y \cdot k_t + b_y \tag{37}$$

Where W_k and b_k are the weights and biases for the hidden state, and W_y and by are the weights and biases for the output. By comparing these models, we aim to determine the most effective approach for predicting stress values from MD simulation data, considering evaluation metrics, model complexity, and computational resources.

2.2.4. Evaluation metrics

When developing a regression model, it is essential to assess its performance using a variety of evaluation metrics. These metrics provide insight into the model's learning and predictive accuracy. Below are descriptions and mathematical expressions for key metrics:

Mean Absolute Error (MAE): MAE measures the average magnitude of errors between paired observations, reflecting the same phenomenon. It is calculated by taking the mean of the absolute differences between predicted values and actual values:

$$MAE = \frac{1}{n}\sum_{i=1}^{n}\left|y_i - y_{pred,i}\right| \tag{38}$$

Root Mean Squared Error (RMSE): RMSE is a quadratic scoring rule that represents the average magnitude of the error. It is the square root of the mean of the squared differences between predicted and actual values:

$$RMSE = \sqrt{\frac{1}{n}\sum_{i=1}^{n}\left(y_i - y_{pred,i}\right)^2} \tag{39}$$

R-squared (R^2): Also known as the coefficient of determination, R2 indicates how well the data fit the regression model. It represents the proportion of the variance in the dependent variable that is predictable from the independent variables:

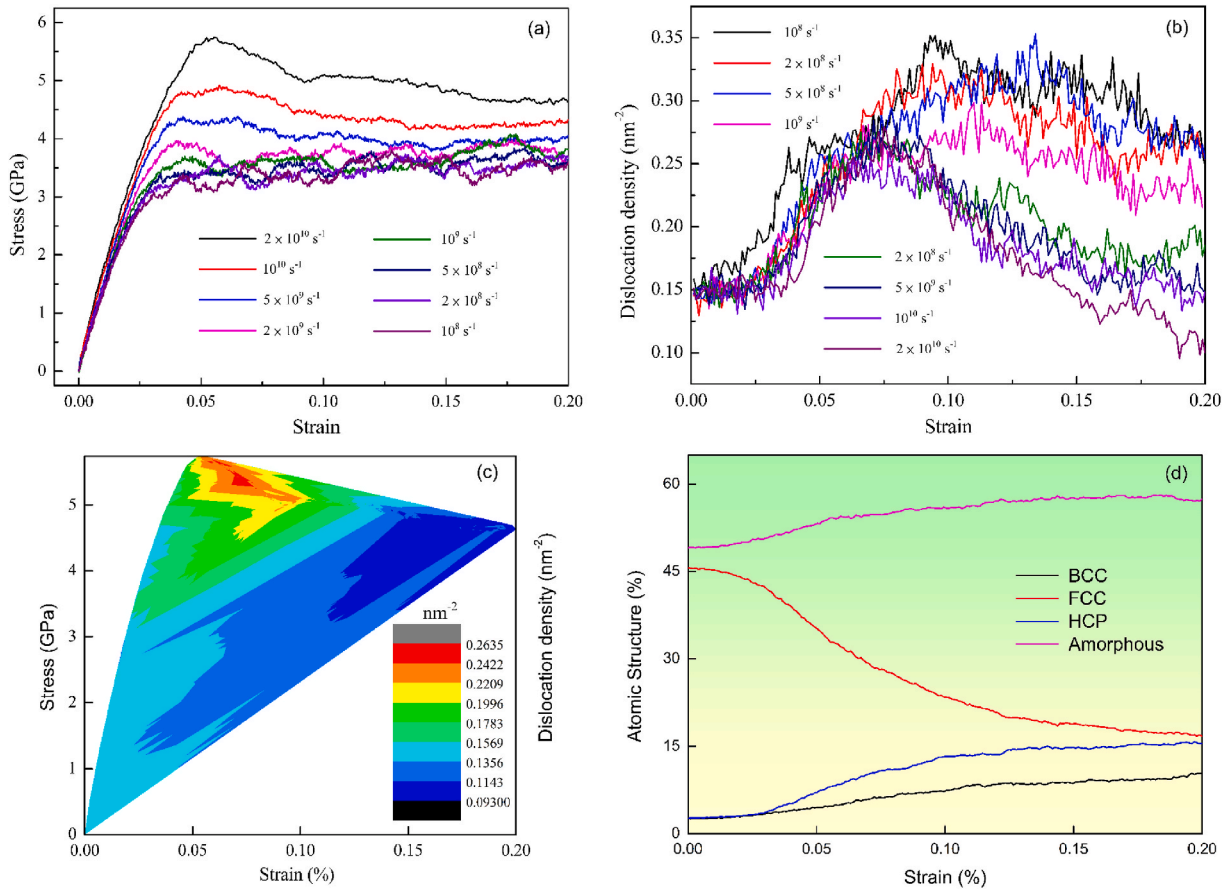

Fig. 2. Stress-strain curves of AlCoCrCuFeNi HEA at various strain rates with a grain size of d = 8.09 nm (a). Evolution of total dislocation density in AlCoCrCuFeNi HEA during tensile deformation at different strain rates (b). Stress-strain-dislocation density (nm^{-2}) diagram for a strain rate of 2×10^{10} s^{-1} at 300K with d = 8.09 nm (c). Evolution of atomic composition in AlCoCrCuFeNi HEA under tensile loading at a strain rate of 5×10^{9} s^{-1} with the grain size of 8.09 nm and 700K (d).

$$R^2 = 1 - \frac{\sum_{i=1}^{n}\left(y_i - y_{pred.i}\right)^2}{\sum_{i=1}^{n}(y_i - \bar{y})^2} \quad (40)$$

Where y_i represents the actual value, $y_{pred,\,i}$ denotes the predicted value, $\bar{y}$ is the mean of the actual values, and n is the number of observations.

2.2.5. *Model interpretability with partial dependence plots*

Partial dependence plots (PDP) are valuable tools for visualizing and analyzing the interaction between the predicted response and input features, thereby enhancing the interpretability of machine learning models [98,99]. These plots demonstrate how the predicted response depends on one or more input features of interest while averaging the effects of other features (referred to as 'complement' features). In essence, partial dependence can be interpreted as the expected model prediction as a function of the input features of interest.

Given the limits of human perception, the set of input features of interest is usually small (typically one or two) and is chosen among the most essential features. One-way PDPs provide insights into the interaction between the predicted response and a single feature of interest, revealing whether the relationship is linear, non-linear, or more complex. By using PDPs, we can capture and understand the relationship between the input features and the prediction output, thereby improving the interpretability of the machine learning model and providing clearer insights into how the model makes its predictions.

Let X_S be the set of input features of interest and X_C be its complement. The partial dependence of the response f at a point x_S is defined as:

$$pd_{X_S}(x_S) \overset{def}{=} E_{X_C}[f(x_S, X_C)] = \int f(x_S, x_C)p(x_C)d(x_C), \quad (41)$$

where f (x_S, x_C) is the response function for a given sample with values defined by x_S for the features in X_S, and by x_C for the features in X_C. One can generate a PDP plot by computing this integral for various values of x_S.

3. Results and discussion

A. Results of MD simulation

3.1. *Impact of strain rate*

Various strain rates have been selected to probe the impact of strain rate on the deformation characteristics of AlCoCrCuFeNi high-entropy alloy specimens. In line with the methodology used in the previous section, a specimen featuring a grain size of d = 8.09 nm and an ambient temperature of 300 K is used to look at the impact of strain rate on the mechanical attributes of the HEA sample.

Fig. 2 (a) illustrates the stress-strain curves of the HEA specimen during tensile testing at various strain rates. The results show that these diagrams are relatively close to each other at the linear elastic stage. It emphasizes that the yield strength increases with an increasing strain rate [100,101], demonstrating a dependence on strain rates, as seen in Fig. 2(a). At elevated strain rates, atoms lack sufficient mobility for bond rearrangement, impeding their response to external forces and thus compromising the replenishment of energy expended in countering applied stresses, leading to diminished yield strength and plastic deformation. This phenomenon aligns with the findings by Ref. [102], who observed a comparable trend in the Al0.3CoCrFeNi HEAs alloy.

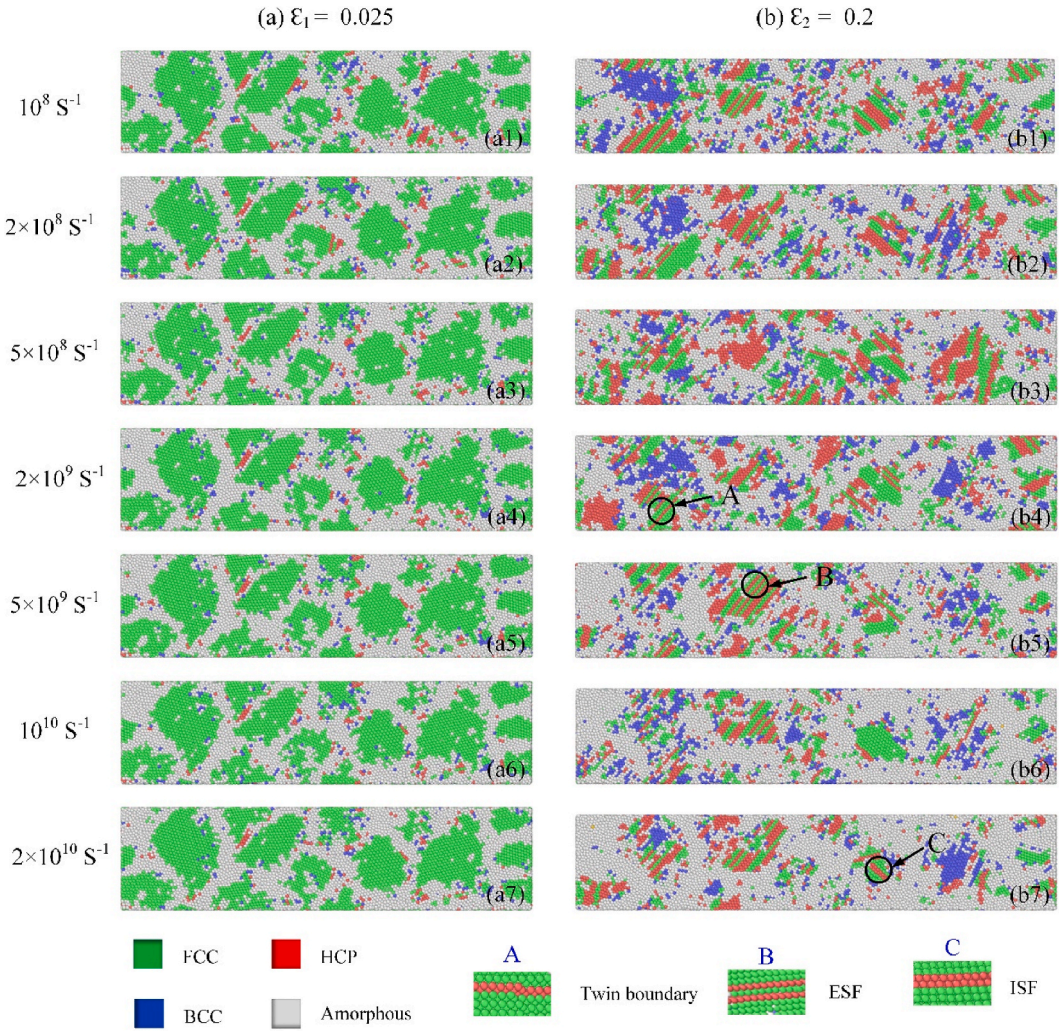

Fig. 3. The CNA of AlCoCrCuFeNi HEA with various strain rate values under tension deformation process.

Fig. 2(a) illustrates the variation of Young's modulus in the AlCoCrCuFeNi HEAs specimen concerning strain rate. Young's modulus gradually increases within the 10^8–10^9 s^{-1} range, with a notable augmentation observed mainly in 10^{10} - 2 × 10^{10} s^{-1}. These results align with the findings of prior investigations conducted by Refs. [103,104]. Fig. 2(b) provides a comprehensive depiction of the impact of strain rates on dislocation evolution. During tension loading, there is a discernible trend of escalating dislocation duration. The continuum of dislocation length spans from the initial phase to the point of yield. Subsequently, there is notable variability in dislocation length during subsequent stages. While there is a modest augmentation in total dislocation length at lower strain rates (ranging from 10^8 to 10^9 s^{-1}), a pronounced increase is observed at higher rates (5 × 10^9–10^{10} s^{-1}). In broad terms, a positive correlation emerges between strain rate and total dislocation length. Consequently, it can be inferred that strain rates exert a significant influence on the mechanical properties and deformation mechanisms of the AlCoCrCuFeNi HEAs alloy during tensile testing. Nevertheless, the influence of strain rate is comparatively lower than that of other factors such as temperature and grain size. Fig. 2(c) illustrates the stress-strain-dislocation density diagram and highlights the complex deformation behavior of the AlCoCrCuFeNi HEA under extreme conditions. The initial high strength reflects the intrinsic resistance of the HEA's multi-elemental structure to deformation, a hallmark of HEAs due to their lattice distortion and solid-solution strengthening. The subsequent softening and high dislocation density indicate that plastic deformation is accommodated by defect generation and possibly localized structural changes, such as amorphization or phase transitions, which are explored further in Fig. 2(d). The nanoscale grain size intensifies these effects, as grain boundaries act as barriers to dislocation motion and serve as sites for defect accumulation. Fig. 2(d) illustrates the dynamic structural evolution of the AlCoCrCuFeNi HEA under tensile loading. The marked decline in the FCC phase suggests that, although initially dominant, this structure is susceptible to destabilization under high strain rates and elevated temperatures. This transition is accompanied by a corresponding increase in the amorphous fraction, likely driven by defect accumulation and thermal activation at 700 K. In contrast, the relative stability of the BCC and HCP phases implies greater resistance to transformation, potentially due to their higher stacking fault energies or reduced sensitivity to shear-induced disorder. The slight increase in the HCP phase may be attributed to deformation twinning or stacking fault formation within the FCC phase mechanisms commonly observed in HEAs during tensile deformation. Fig. 2 (c-d) Provide a comprehensive view of the AlCoCrCuFeNi HEA behavior under extreme tensile loading conditions. Fig. 2(c) highlights the mechanical response and defect evolution, showing that the material undergoes significant plastic deformation with a high dislocation density, leading to strain softening after an initial peak stress. Fig. 2 (d) further illustrates the structural transformations associated with the observed deformation, notably the destabilization of the FCC phase and the increased formation of amorphous regions. The high strain rates (2 × 10^{10} s^{-1} in Figs. 2(c) and 5 × 10^9 s^{-1} in Fig. 2(d)) combined with a grain size of 8.09 nm intensify these effects, accelerating defect generation

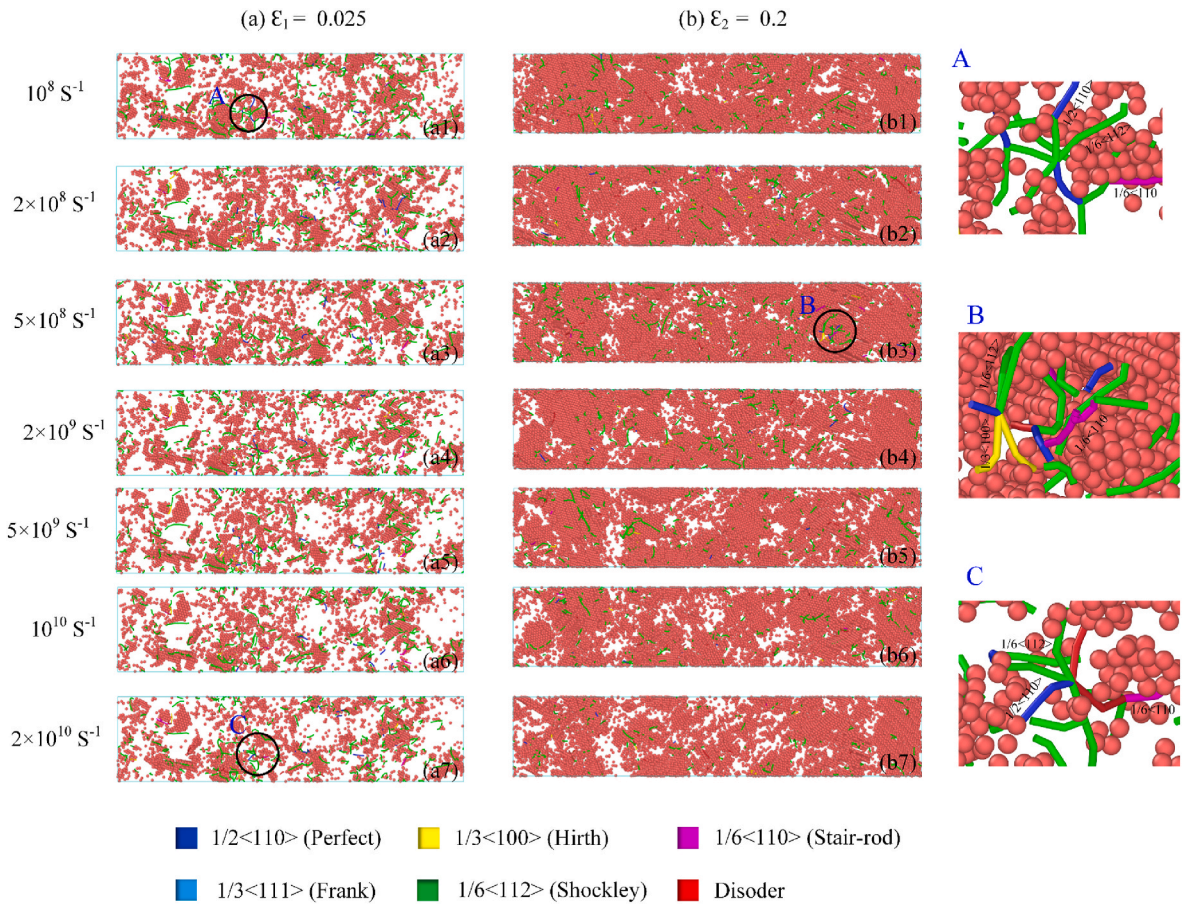

Fig. 4. The dislocation system in the AlCoCrCuFeNi HEA under different strain rates in the tension deformation process.

and promoting structural disorder. Additionally, the temperature difference of 300 K in Fig. 2(c) versus 700 K in Fig. 2(d) plays a critical role, with the elevated temperature in Fig. 2(d) enhancing phase transformation and amorphization processes.

Fig. 3 illustrates the phase transformations occurring in AlCoCrCuFeNi HEA specimens with a grain size of d = 8.09 nm across various strain rates. As stress reaches its peak in Fig. 3(a1-a7), several face-centered cubic structures undergo a transition into hexagonal close-packed and body-centered cubic structures. Notably, the proportion of FCC structures shifting in HEA samples becomes more pronounced with increasing strain rates, evidenced by the significant emergence of HCP and BCC structures in Fig. 3(a4, b4). Furthermore, Fig. 3(a1-b1) depicts the phase transition corresponding to a strain value of $\varepsilon = 0.20$. During this phase, various structures, such as BCC and HCP, were uniformly observed across all tissues analyzed. This observation underscores the pronounced influence of strain rates on the composition of amorphous and HCP structures, with their proportions notably escalating under heightened strain rates. Such augmentation can be attributed to the accumulation of internal stress within the specimen when subjected to elevated strain rates. Consequently, a discernible propensity towards phase transition becomes increasingly apparent with escalating strain rates.

Fig. 4 delineates the progression of dislocation in the AlCoCrCuFeNi HEA model with a lattice parameter of d = 8.09 nm under tensile testing conducted at various strain rates. At low strain levels ($\varepsilon_1 = 0.025$), partial dislocations (green, Shockley) dominate the microstructure, especially in grain interiors, indicating that dislocation nucleation and propagation are the primary carriers of plasticity. As strain increases to $\varepsilon_2 = 0.2$, dislocation density rises significantly, and more complex interactions such as the formation of stair-rod dislocations (purple) and perfect dislocations (dark blue) become evident. At lower strain rates at 10^8 s^{-1}, dislocation activity remains localized, and dislocation lines are more distinct and separated. However, as the strain rate increases to 2×10^{10} s^{-1}, a more disordered structure emerges, with overlapping dislocation networks and enhanced interaction between dislocations. This transition indicates a shift from isolated dislocations to collective motion and entanglement, leading to localized stress concentrations. The subfigures A, B, and C further highlight diverse dislocation types. For instance, the coexistence of Shockley, perfect, and Hirth dislocations (green, dark blue, yellow) in confined regions suggests a high degree of dislocation interaction and transformation, reflecting the complex nature of plastic deformation in HEAs. Notably, stair-rod dislocations indicate junction formation during dislocation reactions, while Frank dislocations (cyan) imply vacancy clustering or void nucleation. Overall, the figure demonstrates that dislocation mechanisms in AlCoCrCuFeNi HEA are highly strain-rate and strain-level dependent. Low strain rates facilitate dislocation nucleation and glide, while high strain rates promote dislocation multiplication, interaction, and structural disorder. This behavior underscores the need to tailor strain rate conditions to achieve desirable mechanical performance in HEAs. As anticipated, there is a notable escalation in the proportion of dislocations with rising strain rates, as depicted in Fig. 4(a1-a7). The findings also show that the Shockley dislocation is dominant in the evolution of dislocations. The grain interior looked denser at strain rates of 5×10^9 and 10^{10} s^{-1}. Thus, the strain rate significantly impacts the development and progression of dislocations [105,106].

Fig. 5 illustrates the distribution of atomic shear strain in AlCoCrCuFeNi models with a diameter of 8.09 nm under stress testing at 300 K and various strain rates. The findings indicate that elevated Von Mises shear stress values tend to concentrate more prominently at grain

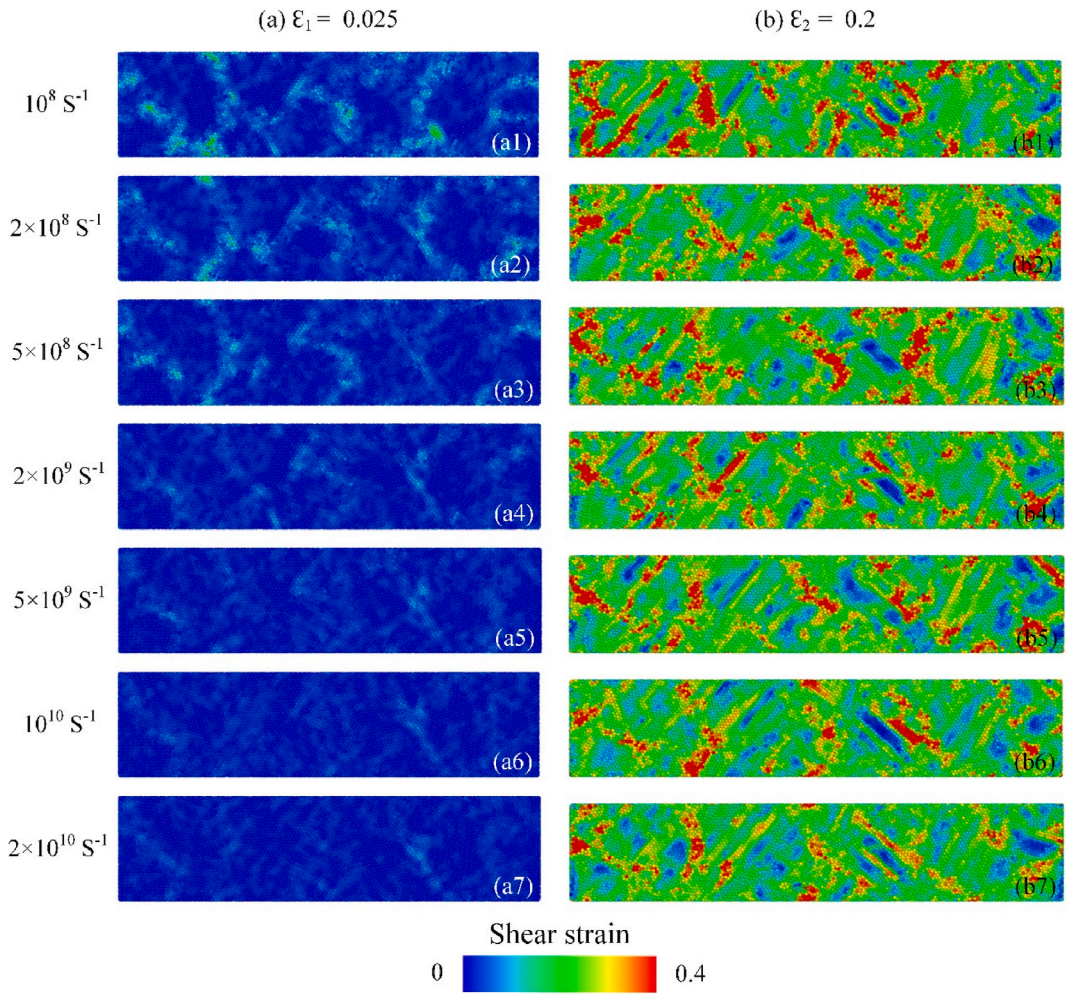

Fig. 5. The shear strain distribution of AlCoCuCrFeNi HEA with different strain rates under the tensile process.

boundaries (GB) at the onset of yielding, as evidenced in Fig. 5(a1–a7). The onset of early deformation appears to initiate at grain boundaries (GBs), characterized by their lower atom density. As strain increases, Von Mises shear stress (VMSS) within grain interiors rises, indicating the initiation of phase transformations in Fig. 3 (b1–b7). Additionally, Fig. 2 (b) shows that local VMSS decreases with higher strain rates. VMSS reflects atomic mobility under loading; thus, limited relaxation time at elevated strain rates results in reduced VMSS. Moreover, higher strain rates enhance yield strength and dislocation density while restricting atomic mobility, which limits bond rearrangement and plastic deformation. These findings underscore the potential of designing strain-rate-sensitive HEAs for high-speed impact and aerospace applications.

3.2. *Impact of grain size and temperature*

This subsection delves into the influence of grain sizes and temperature variations on the mechanical properties and deformation mechanisms of AlCoCrCuFeNi HEA. Tension tests were conducted on samples with varying grain sizes and temperatures with a strain rate of 10^9 s^{-1}.

As depicted in Fig. 6(a), a stress-strain curve exhibits both elastic and plastic phases. Initially, in the elastic regime (stage I), the stress rises linearly until reaching the yield strength value at strain levels ranging from 0.035 to 0.05, depending on the grain size. During the subsequent plastic deformation stage (stage II), the stress consistently diminishes for all grain sizes. Beyond a strain of 0.075, the tensile stress stabilizes, becoming less reliant on strain, indicative of flow stress. Flow stress was determined as the average stress within the strain range of 0.075–0.2. Prior investigations have emphasized the significant influence of grain size d on flow stress in the plastic domain, highlighting the role of grain boundaries (GB) motion and dislocation propagation [107–109]. Fig. 6 (c) presents a stress-strain-dislocation density (nm^{-2}) diagram for the AlCoCrCuFeNi high-entropy alloy (HEA) under a strain rate of 10^9 s^{-1} at 300 K, with a grain size of 7.07 nm. The contour plot illustrates the relationship between stress (0–4 GPa), strain (0–0.2), and dislocation density (0.1109–0.2635 nm^{-2}), revealing peak stress of approximately 4 GPa at a strain of 0.05, followed by a gradual decline to about 2 GPa, indicative of strain softening. Concurrently, the dislocation density increases from 0.1109 nm^{-2} at low strains to a maximum of 0.2635 nm^{-2} at higher strains, reflecting significant defect accumulation driven by the high strain rate and nanoscale grain size, which limits recovery mechanisms. In contrast, Fig. 6(d) depicts the evolution of atomic composition in the same HEA under tensile loading at a strain rate of 10^9 s^{-1}, a temperature of 300 K, and a slightly larger grain size of 10.19 nm. The plot tracks the fractions of BCC, FCC, HCP, and amorphous phases, showing a marked decrease in the FCC phase from approximately 45 % to about 15 % with increasing strain. In contrast, the amorphous phase increases from approximately 5 %–10 %, while the BCC and HCP phases remain relatively stable at around 10 % and 5 %, respectively. This indicates that the FCC structure undergoes deformation-induced amorphization, likely driven by high strain rates and limited thermal activation at 300 K, highlighting the alloy's structural instability under such conditions.

The graphical representation in Fig. 7 delineates the transformation of the face-centered cubic crystalline structure into hexagonal close-

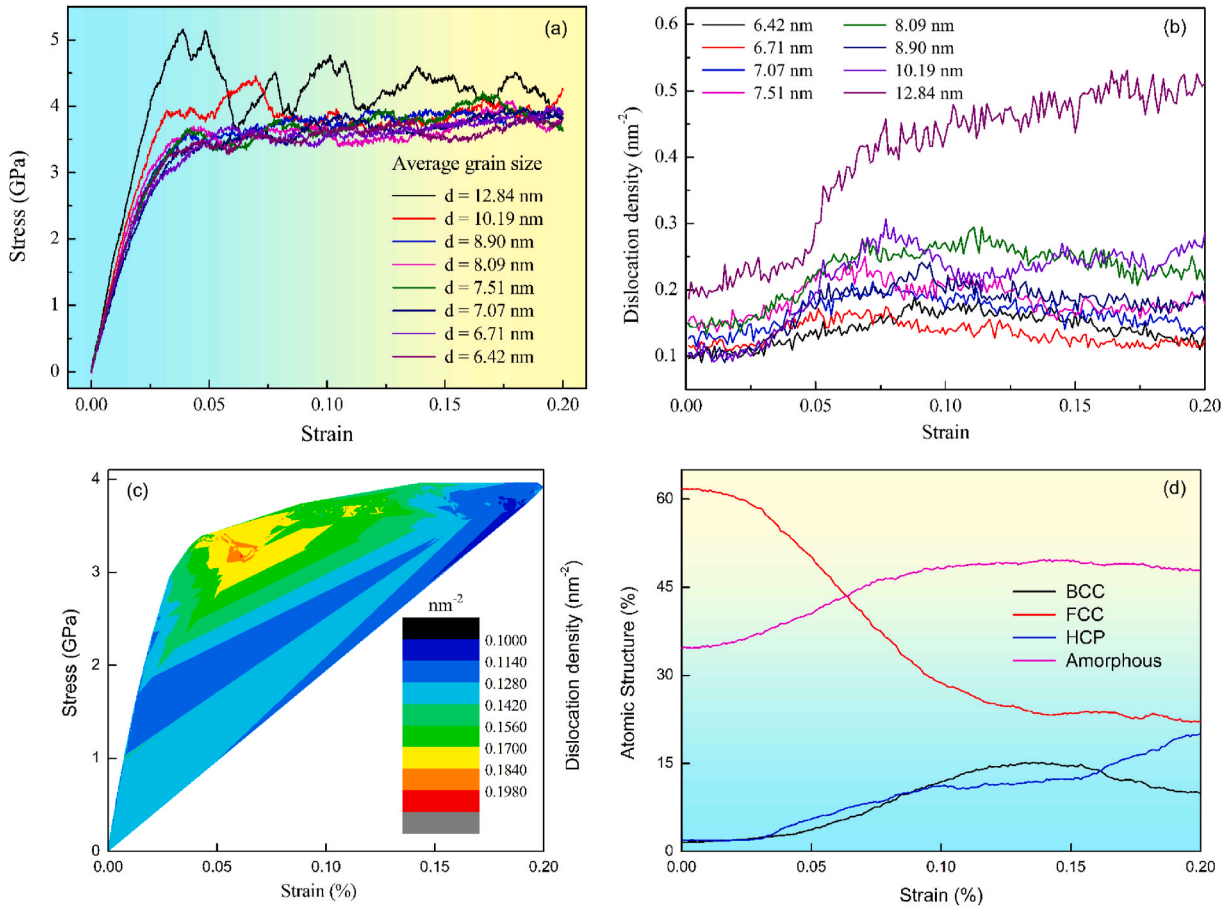

Fig. 6. Stress-strain curves for polycrystalline AlCoCrCuFeNi HEA at various grain sizes with a strain rate of 10^9 s^{-1} (a). Evolution of total dislocation density in AlCoCrCuFeNi HEA during tensile deformation at various grain sizes (b). Stress-strain-dislocation density (nm^{-2}) diagram for a strain rate of 10^9 s^{-1} at 300K with d = 7.07 nm (c). Evolution of atomic composition in AlCoCrCuFeNi HEA under tensile loading at a strain rate of 10^9 s^{-1} with grain size at 10.19 nm and 300K (d).

packed, body-centered cubic, and amorphous configurations during the tensile process. Concurrently, elastic energy accumulation within the material is progressive as strain levels escalate. Beyond the yield point, observations indicate a discernible transition within the polycrystalline specimen from the predominant FCC arrangement to a combination of HCP, BCC, and amorphous phases, attributable to the substantial dissipation of stored elastic energy across all samples. This empirical observation aligns with the findings elucidated in a prior investigation by Ref. [110], which examined the evolution of microstructures in both pure tungsten and graphite-tungsten composite samples. Fig. 7(a) elucidates the fundamental deformation characteristics within the inverse H-P region. The captured figure reveals that Shockley partial dislocations dominate the dislocation structure, particularly within grain interiors. This suggests that partial dislocation activity is the primary mechanism driving plastic deformation under the given conditions. This is especially notable considering the small grain diameter of 6.42 nm, which contrasts sharply with the significantly larger diameter of 12.48 nm.

Fig. 8 depicts the rotation of specific grains under increasing strain, highlighted by black ellipses labeled a1–a4. Concurrently, grain boundary (GB) migration is observed with elevated strain levels, indicated by black rectangles b1–b4. These phenomena suggest that, in the inverse Hall–Petch regime, plastic deformation is primarily driven by the synergistic mechanisms of grain rotation and GB migration, in agreement with previous studies by Chen et al. [111] and Vu et al. [112]. Grain rotation and GB migration were identified through the sequential analysis of atomic configurations, where noticeable grain reorientation (a1–a4) and boundary displacement (b1–b4) were evident as strain progressed.

The dislocation distribution within the AlCoCrCuFeNi high-entropy alloys model with grain sizes ranging from 6.42 nm to 12.84 nm under tension testing conditions at 300 K, specifically at strain levels of 0.05 and 0.20. Subfigures (a1-a8) within Fig. 8 depict the dislocation patterns observed in the AlCoCrCuFeNi HEA specimens at a strain level of 0.05. Notably, due to the polycrystalline nature of the material, dislocations are primarily confined to grain boundaries (GBs) before the initiation of tensile simulation. This occurrence can be attributed to the distinct crystal orientations within each grain, leading to atomic rearrangements and orientation shifts at the interfaces of these grain boundaries. Consequently, lattice discontinuities arise, facilitating the entrapment of dislocations at these interfaces.

As depicted in Fig. 6(b), the dislocation density is not initiated at zero upon the commencement of the tension test. After the strain reaches $\varepsilon = 0.2$, Fig. 9 (b1-b8) illustrates the distribution of dislocations. With increasing grain size, there is a notable augmentation in dislocation formation along the grain boundary and their subsequent propagation within the grain interior, accompanied by a pronounced phase transition. When subjected to tension loading, dislocations extend and engage with the grain boundaries, resulting in their deterioration, mutual reaction, the genesis of new dislocations, or absorption by adjacent grain boundaries. Empirical observations indicate that dislocation density within the grain interior is notably higher in specimens with larger grain sizes than in those with smaller ones. Moreover, these precipitate dispersions exhibit extended durations, encompassing broader scopes, and demonstrate increased particulate dimensions. The Shockley partial dislocation emerges as the prevailing configuration across all instances

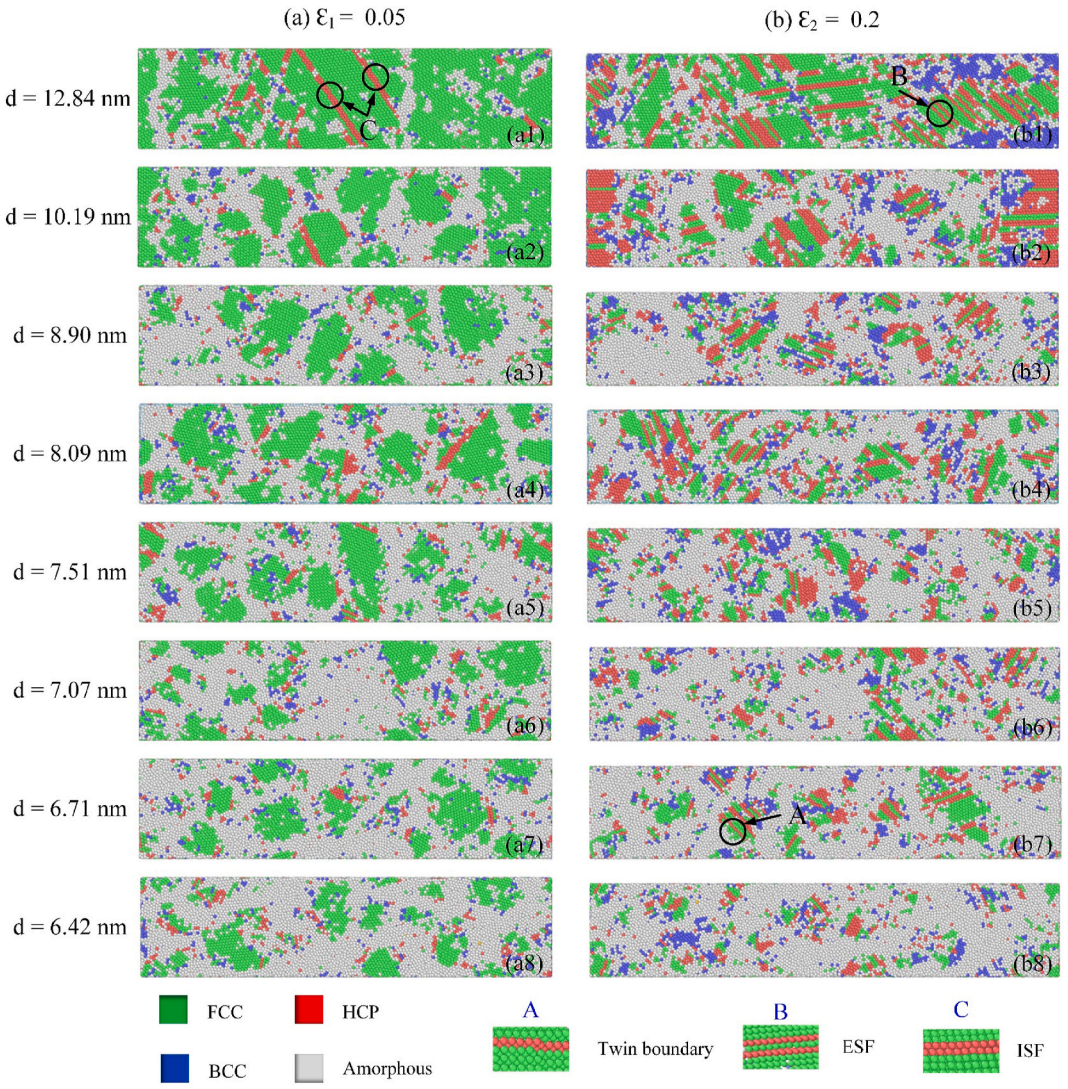

Fig. 7. The CNA of polycrystalline of AlCoCrCuFeNi HEA with different grain size values under tension process.

[113]. Fig. 6(b) presents the dislocation density characterization of AlCoCrCuFeNi HEA within series d, providing insight into dislocation evolution. Initially (Stage I), dislocations predominantly localize at grain boundaries (GB), resulting in higher dislocation densities in smaller grain sizes due to elevated GB densities, as observed in Fig. 8 (a1-a8). Subsequently, during plastic deformation (Stage II), dislocation density experiences a rapid escalation within the Hall-Petch (H-P) region associated with grain size while exhibiting near-constant levels across the spectrum from d = 6.42 nm–10.19 nm, with a marginal increase observed for d = 12.84 nm towards the latter stages. In materials characterized by small grain sizes, the absence of phase transitions stems from grain rotation and grain boundary (GB) motion, collectively contributing to a consistent dislocation density. Conversely, in inverse Hall-Petch (H-P) relationships, grain boundary (GB) migration and grain rotation emerge as the principal deformation mechanisms. In contrast, conventional H-P relationships are characterized by dislocation activity as the primary deformation feature. Concurrently, stacking faults (SF) and precipitate dispersions (PD) are continually generated and assimilated by the GB, thereby fostering an augmentation in dislocation density during the tensile process, particularly evident in instances featuring larger grain sizes.

The evaluation of pivotal deformation mechanisms within the Hall-Petch (H-P) and inverse H-P regimes necessitates the calculation of local von Mises shear strain (VMSS), as outlined in Ref. [114]. Fig. 9 delineates the gradual deformation progression under varied strain conditions for diverse grain sizes, with grain sizes spanning from d = 6.42 nm to d = 12.84 nm as indicative of the inverse H-P and H-P regimes, respectively. Remarkably, the visual representation employs color differentiation for atoms contingent upon their corresponding local VMSS values, with red indicating elevated VMSS values. Fig. 9 (a2-b2) illustrates the localized Von Mises stress at the yield point, revealing a notably high initial VMSS value concentrated at the grain boundary (GB). This observation implicates the GB predominantly in the initial deformation process of the AlCoCrCuFeNi HEA specimen. However, it is discerned that the extent of the GB's influence varies between the two specimens under scrutiny. Notably, in the case of the specimen featuring a grain size of d = 6.42 nm in Fig. 9(a7-b7), the heightened VMSS is primarily localized at the GBs. The progression of strain is accompanied by the detection of GB migration and grain rotation, as evidenced by the sequential evolution from black ellipse a1 to a8 and rectangle b1 to b8 in Fig. 7. This observation strongly suggests that the primary mechanism governing deformation involves grain rotation and GB migration. As the grain size (d) reaches 12.84 nm, a substantial Von Mises stress is prominently evident both at the grain boundary (GB) and along the glide plane within the grain interior, correlating with increasing strain levels. These phenomena explain the evolution and transition of phases and dislocations observed in Fig. 7, particularly in configurations associated with larger grain sizes (d). Consequently, the

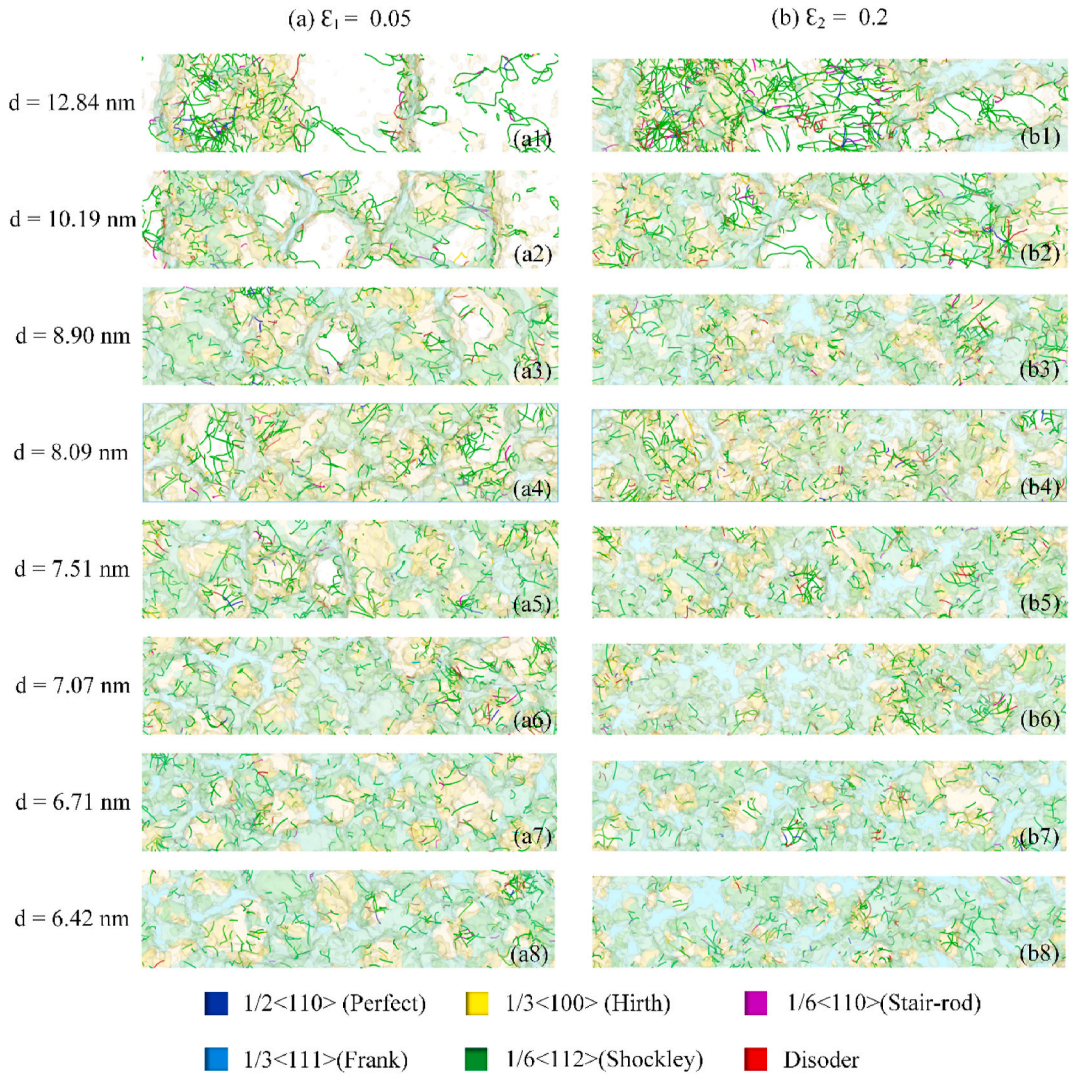

Fig. 8. The dislocation distribution of AlCoCrCuFeNi HEA with various grain sizes under the tension process.

progressive phase transitions contribute to the elevation of VMSS within the grain interior concurrent with the augmentation of grain size [115]. The transition from Hall-Petch to inverse Hall-Petch behavior was identified. While finer grains enhance strength due to grain boundary strengthening, they suppress dislocation activity; in contrast, coarser grains facilitate dislocation propagation. These findings offer valuable guidance for optimizing grain size in nanostructured HEAs to balance strength and ductility.

Fig. 10(a) illustrates a stress-strain-dislocation density (nm^{-2}) diagram for the AlCoCrCuFeNi HEA under a strain rate of 10^9 s^{-1} at 700 K, with a grain size of 7.07 nm. The contour plot reveals the interplay between stress (0–3 GPa), strain ε = (0–0.2), and dislocation density (0.0900–0.2435 nm^{-2}), showing peak stress of approximately 3 GPa at a strain ε = 0.05, followed by a gradual decline to 1.5 GPa, indicative of strain softening likely due to dynamic recrystallization or phase transformations at the elevated temperature. The dislocation density increases from 0.0900 nm^{-2} at low strains to a maximum of 0.2435 nm^{-2} at higher strains, reflecting significant defect accumulation driven by the high strain rate and nanoscale grain size, which restricts recovery mechanisms despite the higher temperature. Complementing this, Fig. 10(b) depicts the evolution of dislocation density (nm^{-2}) under tensile loading across various temperatures (300 K–1000 K) for AlCoCrCuFeNi HEA. The plot shows multiple curves, each representing a different temperature, with dislocation density generally peaking between 0.15 and 0.25 nm^{-2} at strains ε = (0.05–0.10), followed by fluctuations that suggest dynamic interactions between dislocation generation and annihilation. Notably, higher temperatures exhibit slightly lower peak dislocation densities and more pronounced fluctuations, likely due to enhanced thermal activation facilitating recovery processes such as dislocation climb and annihilation, providing insight into the temperature-dependent deformation behavior of the AlCoCrCuFeNi HEA. In addition, the evolution of dislocation density within AlCoCrCuFeNi high-entropy alloy specimens characterized by diverse grain dimensions facilitates a comprehensive examination of sample advancement. In an earlier study [116], dislocation density was determined by quantifying the cumulative length of dislocations per unit volume. The dislocation density curves exhibit a notable surge across all samples until the material attains its yield point. The density of dislocations gradually increases with significant fluctuations throughout the remainder of the stress period.

Fig. 11. Presents the von Mises shear strain distribution across AlCoCrCuFeNi high-entropy alloy specimens at various temperatures during stress testing conducted at a strain rate of 10^9 s^{-1} and with a grain size (d) of 8.09 nm. Atom coloring corresponds to VMSS values, with red indicating the highest von Mises shear strain. The initial snapshot depicts the specimen's yield point. Subsequent snapshots in Fig. 11(a1-a8) illustrate that an increase in strain rate corresponds to a concurrent rise in yield strain. The local shear strain begins to nucleate

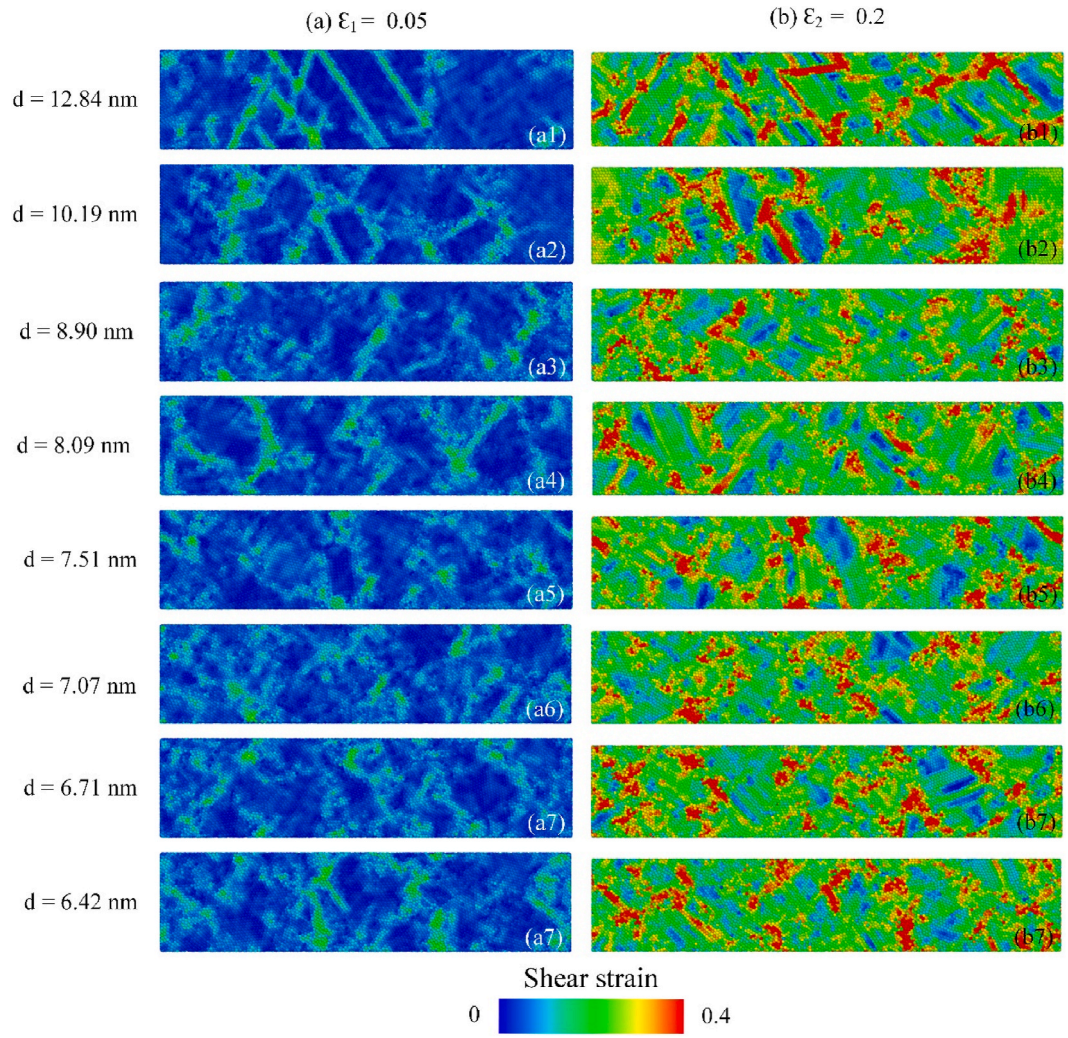

Fig. 9. The shear strain distribution of AlCoCuCrFeNi HEA with different grain sizes under tension process.

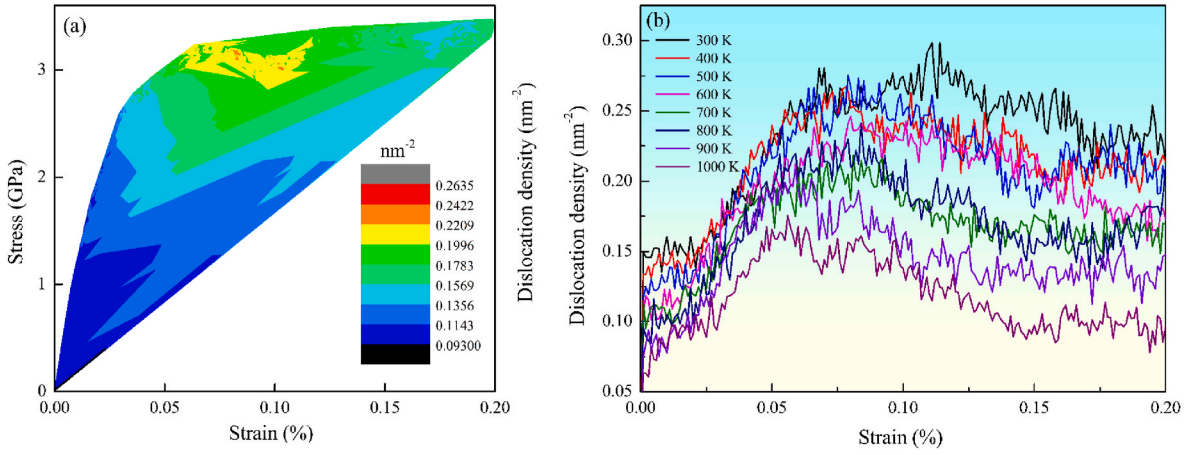

Fig. 10. Stress-strain-dislocation density diagram for a strain rate of 10^9 s^{-1} at 700K with grain size d = 7.07 nm (a). The dislocation density under the tension process with various temperatures of AlCoCrCuFeNi HEA (b).

at the TB zone and spreads across the grain until it is blocked by neighboring TBs, resulting in shear bands. The second snapshot depicts the deformation at a strain of 0.2, as seen in Fig. 11(b1-b8). The shear strain reduces as the strain rate increases. It can be explained that atoms do not have enough time to cause bond rearrangement at high strain rates. Hence, the atoms with high shear strain values decrease as strain rates increase. Elevated temperatures result in material softening, decreased yield strength, and increased amorphization, underscoring the importance of thermal stability in maintaining mechanical performance under high-temperature conditions.

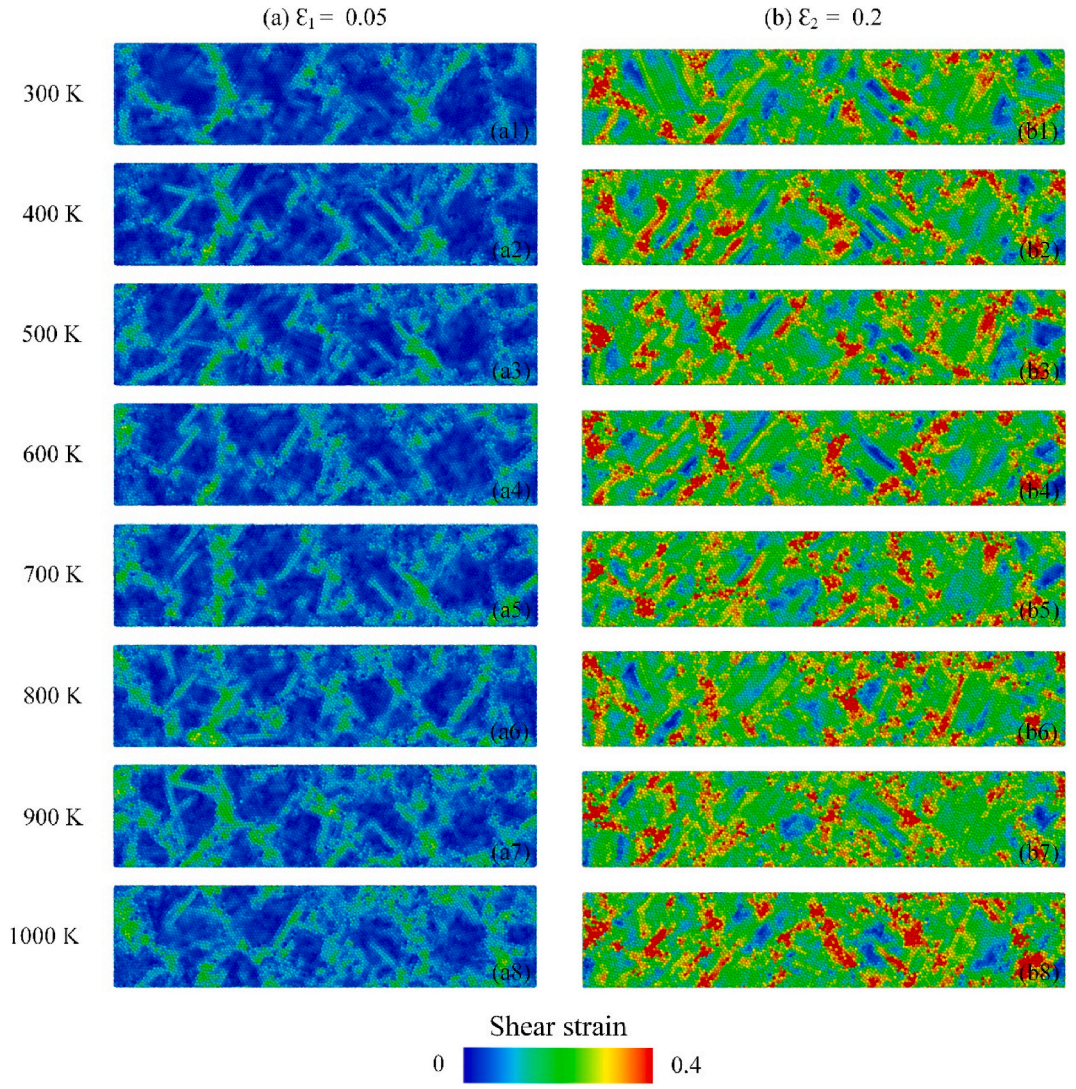

Fig. 11. The shear strain distribution of AlCoCuCrFeNi HEA with different temperatures under the deformation process.

Table 3
Hyperparameters and model configurations.

Hyperparameters	RNN	CNN	BiLSTM	LSTM	FFNN	GRU
Hidden layers	3	4	3	3	3	3
Neurons number	400	356	400	400	400	400
Batch size	20	32	20	32	32	20
Dropout	0.25	0.25	0.25	0.25	0.25	0.25
Learning rate	10^{-4}	10^{-4}	10^{-4}	10^{-4}	10^{-4}	10^{-4}
Optimizer	Adam	Adam	Adam	Adam	Adam	Adam
Total parameters	802001 (3.06 MB)	128161 (500.63BKB)	8973601 (34.23 MB)	3206801 (12.23BM)	323201 (1.23 MB)	2408801 (9.19 MB)

The observed phenomenon can be attributed to a notable augmentation in phase transformation from the FCC phase to an alternative structure after stress peaks, thereby leading to a delayed expansion of dislocation density. Furthermore, the data indicate a positive correlation between dislocation density and temperature, aligning with the dynamic response exhibited by the samples.

B. Results of machine learning

Table 3 presents a detailed comparison of hyperparameters across six deep learning models: Feed Forward Neural Network (FFNN), Convolutional Neural Network (CNN), Long Short-Term Memory (LSTM), Bidirectional Long Short-Term Memory (BiLSTM), Gated Recurrent Unit (GRU), and Recurrent Neural Network (RNN). The FFNN is configured with three hidden layers of 400 neurons each, a batch size of 32, a dropout rate of 0.25, and a learning rate of 10^{-4}, optimized by Adam, resulting in 323,201 parameters (1.23 MB). The CNN model includes four hidden layers with 356 neurons, a batch size of 32, a dropout rate of 0.25, and a learning rate of 10^{-4}, optimized by Adam, totaling 3,206,801 parameters (12.23 MB). The BiLSTM model, equipped with bidirectional layers, consists of 3 hidden layers with 400 neurons each, a batch size of 20, a dropout rate of 0.25, a learning rate of 10^{-4}, and utilizes the Adam optimizer. It has the highest parameter count among models, totaling 8,973,601 (34.23 MB), indicating the greatest model

Table 4
Comparative analysis of machine learning predictive models for stress values (stage 1).

Evaluation	LR	SVR	GBR	FFNN	CNN	LSTM	BiLSTM	GRU	RNN
MAE	0.422	0.202	0.91	0.092	0.178	0.072	0.055	0.047	0.048
RMSE	0.615	0.298	1.25	0.12	0.267	0.095	0.073	0.063	0.063
R^2	0.1	0.85	0.98	0.98	0.9	0.99	0.99	0.995	0.995

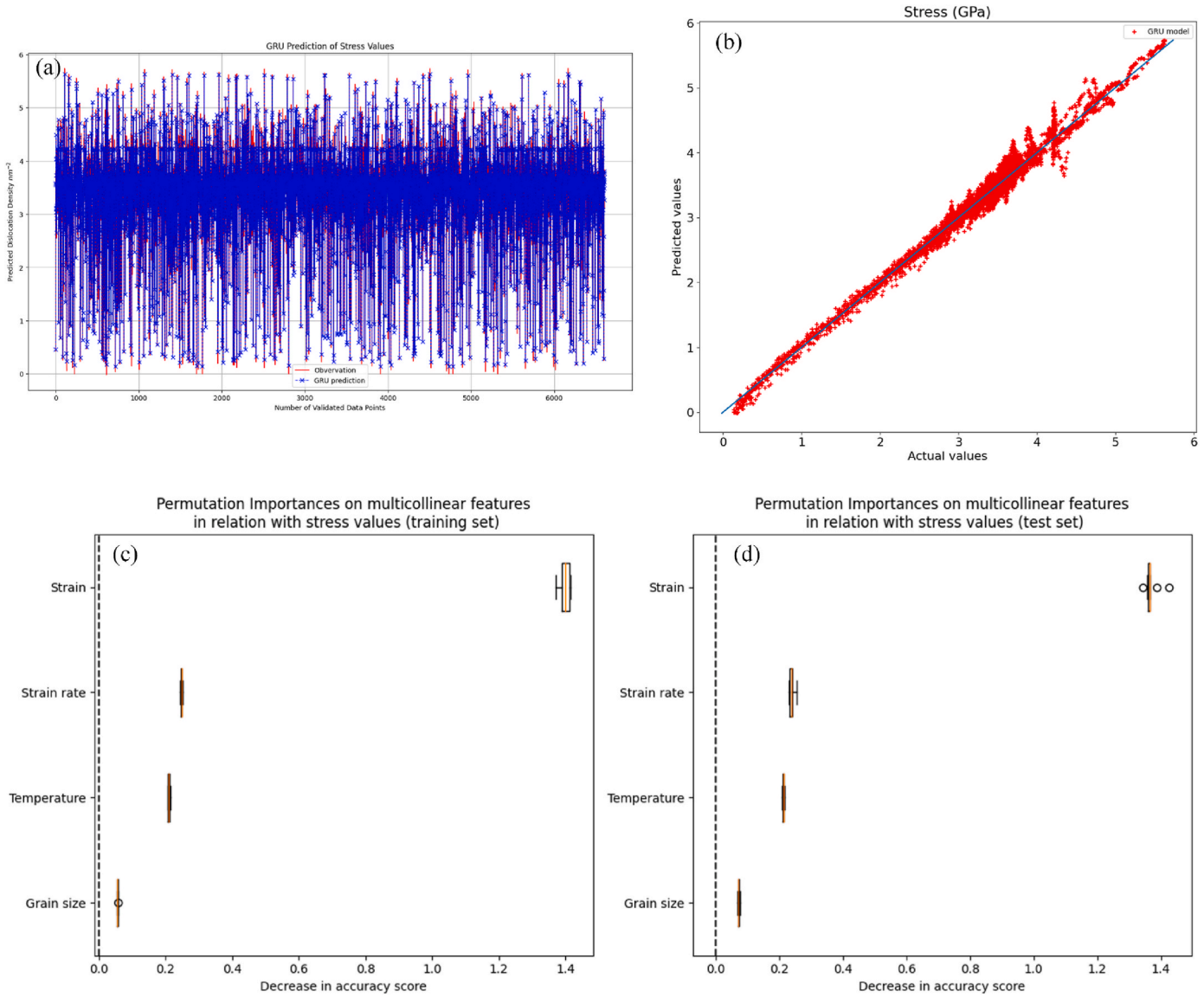

Fig. 12. The significance of features in tensile deformation during the training process (a) and validation (b). The stress prediction from the GRU model (c) and the variance of the GRU model prediction for stress values compared to actual observation (d).

complexity. In comparison, the GRU model also has 3 hidden layers with 400 neurons, a batch size of 20, a dropout rate of 0.25, a learning rate of 1e-4, and the Adam optimizer, with a total of 2,408,801 parameters (9.19 MB). The RNN model, with similar settings, holds 802,001 parameters (3.06 MB), marking it as the least complex. This comparison underscores the BiLSTM model's greater complexity due to its parameter volume, with the RNN as the simplest by this metric. Among the evaluated models, the GRU architecture achieved the highest predictive accuracy, with an R^2 of 0.995, MAE of 0.047, and RMSE of 0.063, demonstrating its robustness in learning complex relationships from MD data.

3.3. Experimental results

Table 4 presents the performance comparison of various machine learning models for stress value prediction during Stage 1. The GRU model demonstrates the best performance, with the lowest Mean Absolute Error (MAE) of 0.047 and Root Mean Square Error (RMSE) of 0.063. Additionally, it achieves the highest R-squared (R^2) value of 0.995, indicating excellent predictive accuracy and minimal error. This highlights the superior performance of the GRU model compared to other models, including LR, SVR, GBR, FFNN, CNN, LSTM, BiLSTM, and RNN, in predicting stress values.

Additionally, Fig. 12(a–b) above highlights the GRU model's

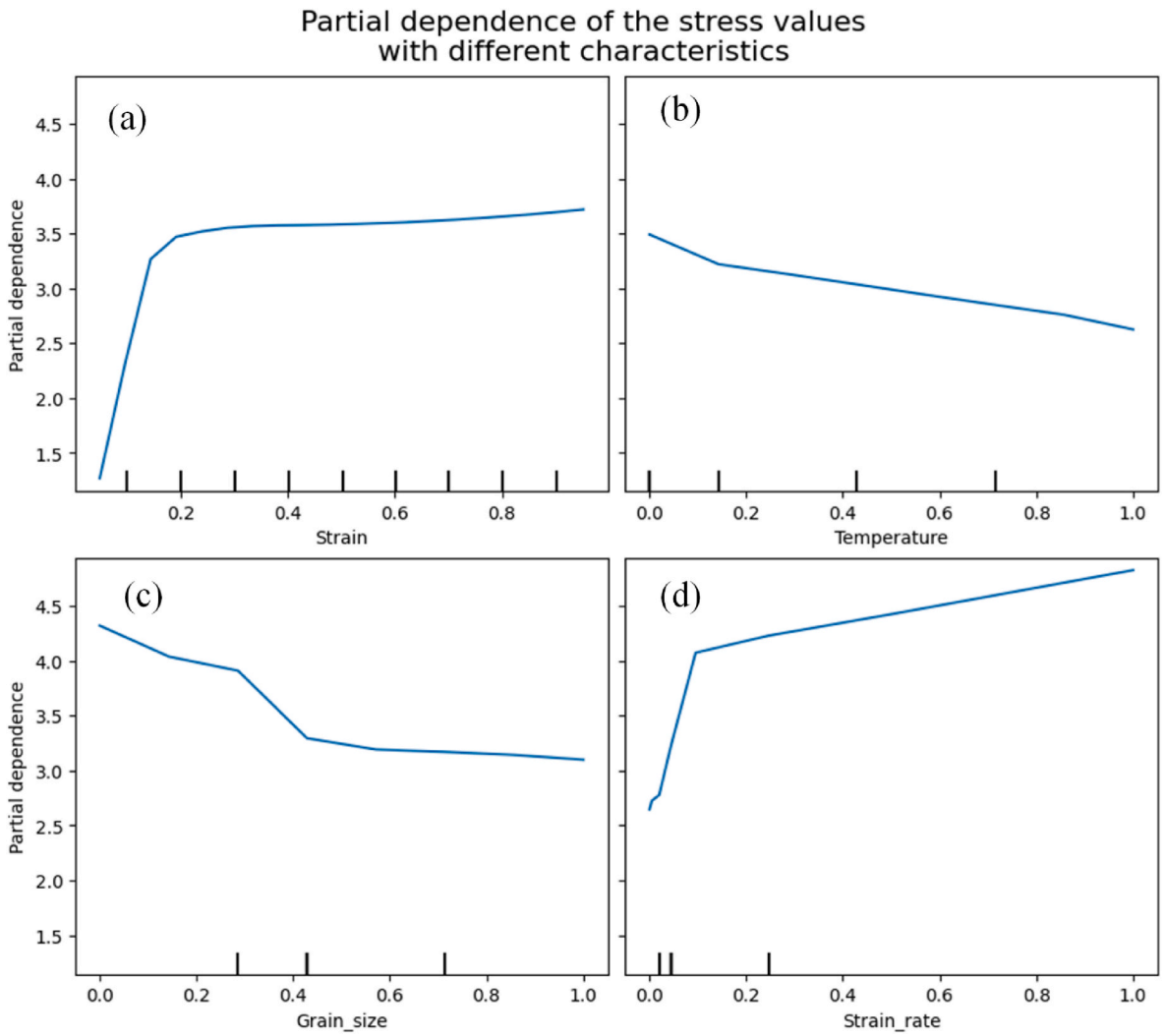

Fig. 13. The partial dependence between the stress values and a set of features of interest.

superior performance in predicting the HEA material's stress values. Fig. 12(a) illustrates a scatter plot of predicted and actual stress values, showing the GRU model's performance. The red crosses represent the predicted values by the GRU model, while the blue line indicates the perfect prediction line where predicted values equal actual values. The close alignment of the red crosses along the blue line demonstrates the high accuracy of the GRU model in predicting stress values with minimal deviation from the actual values. Fig. 12(b) displays the GRU model's prediction of stress values over a large dataset. The plot shows the predicted dislocation density versus the number of validated data points. Blue stars represent the GRU model's predictions, while red crosses indicate the observed values. The GRU model's predictions closely follow the observed values, showcasing its ability to accurately capture the variance and trends within the data. The model maintains high predictive accuracy across the entire range of data points, further emphasizing its robustness and effectiveness in handling complex mechanical property predictions for HEA materials. These figures underscore the GRU model's superior performance in accurately predicting stress values, demonstrating its capability to learn and generalize well from the provided data.

Fig. 12(c–d) above shows the importance of permutation on multicollinear features concerning stress values for the training set (c) and the test set (d). In this analysis, the most important feature for predicting stress is identified as strain, indicated by the most significant decrease in accuracy score when this feature is permuted. Conversely, grain size is the least important feature, exhibiting the most minor decrease in accuracy score upon permutation. The other features, strain rate and temperature, are of intermediate importance. The feature importance ranking remains consistent across the training and test sets. Strain consistently emerges as the most critical feature, followed by strain rate, temperature, and grain size. This consistency signifies that the model effectively understands the hidden representations of the features, capturing the relationship between the input features and the output (stress) reliably. Such robustness in maintaining feature importance across different datasets underscores the model's capability to generalize and produce accurate predictions.

Fig. 13 presents partial dependence plots (PDPs) that illustrate the relationships between the input features (strain, temperature, grain size, and strain rate) and the predicted stress values, helping to discern whether these correlations are linear or non-linear. The plot for strain shows a steep initial increase in stress values up to about 0.2 strain, followed by a more gradual rise, indicating a non-linear relationship where the stress response is more sensitive at lower strain levels. The temperature plot reveals a nearly linear negative correlation, with stress values decreasing consistently as temperature increases. Grain size exhibits a non-linear negative relationship with stress, where stress decreases sharply at smaller grain sizes and tapers off at larger sizes. The strain rate plot also indicates a non-linear relationship, with a sharp initial increase in stress that becomes more gradual at higher strain rates. These PDPs highlight the complex interplay of factors affecting

Table 5
Performance comparison for machine learning predictive models trained directly.

Evaluation	LR	SVR	GBR	FFNN	CNN	LSTM	BiLSTM	GRU	RNN
MAE	0.041	0.04	0.074	0.042	0.02	0.027	0.03	0.036	0.02
RMSE	0.053	0.048	0.1	0.053	0.028	0.329	0.399	0.0453	0.0256
R^2	−0.11	0.22	0.94	0.229	0.81	0.743	0.47	0.28	0.873

Table 6
Evaluation of machine learning predictive models using a pre-trained model.

Evaluation	LR	SVR	GBR	FFNN	CNN	LSTM	BiLSTM	GRU	RNN
MAE	–	–	–	0.399	0.11	0.397	0.075	0.009	0.069
RMSE	–	–	–	0.073	0.0196	0.074	0.101	0.011	0.0129
R^2	–	–	–	0.92	0.82	0.92	0.93	0.973	0.93

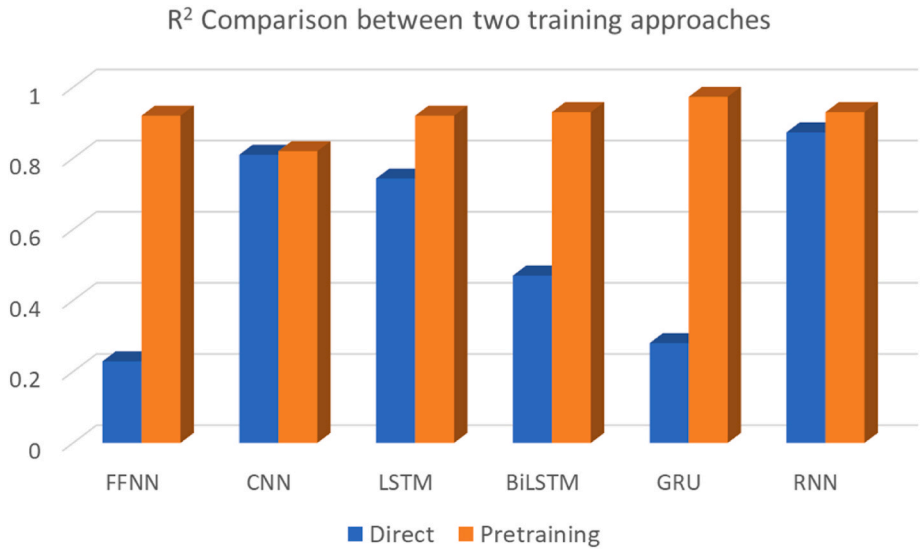

Fig. 14. The R^2 comparison between two approaches, direct training and using the pre-trained model to predict dislocation values.

stress predictions, with strain and strain rate showing strong non-linear relationships, temperature displaying a linear correlation, and grain size having a diminishing negative effect. This detailed understanding enhances the interpretability of the model's predictions.

Table 5 presents the performance comparison of various machine learning models when directly trained to predict dislocation values from Stage 2. The CNN model stands out with the best performance, achieving the lowest Mean Absolute Error (MAE) of 0.02, the lowest Root Mean Square Error (RMSE) of 0.028, and a high R-squared (R^2) value of 0.81, indicating effective predictive accuracy. In contrast, all other models exhibited poor performance. For instance, LR, SVR, GBR, FFNN, LSTM, BiLSTM, GRU, and RNN models failed to achieve similarly low MAE and RMSE values, with the LR model even showing a negative R^2 value of −0.11, indicating a model worse than a simple mean prediction. Except for CNN, this poor performance across models highlights the challenges machine learning algorithms face in learning data representation with limited data, resulting in inadequate predictions. This underscores the difficulty of training models directly on the dislocation dataset from Stage 2, where limited data impacts most algorithms' learning and predictive capabilities.

Table 6 demonstrates the significant benefits of using transfer learning for predicting dislocation values by fine-tuning pre-trained models from Stage 1 on the limited dataset of Stage 2. This approach markedly improves the performance of all models compared to training directly on the limited data. The FFNN model shows improvement with an MAE of 0.399, RMSE of 0.073, and an R^2 value of 0.92. The CNN model demonstrates significant enhancement with an MAE of 0.11, RMSE of 0.0196, and an R^2 value of 0.82. The LSTM model also improves, achieving an MAE of 0.397, an RMSE of 0.074, and an R^2 value of 0.92. The BiLSTM model performs better with an MAE of 0.075, RMSE of 0.101, and an R^2 value of 0.93. The GRU model shows the best performance, with an MAE of 0.009, RMSE of 0.011, and an R^2 value of 0.973, indicating excellent predictive accuracy. The RNN model also benefits from transfer learning, with an MAE of 0.069, RMSE of 0.0129, and an R^2 value of 0.93. The LR, SVR, and GBR models did not apply in this scenario. This table highlights the effectiveness of transfer learning, where leveraging pre-trained models from Stage 1 and fine-tuning them on the Stage 2 dataset leads to significant performance improvements. Notably, the GRU model performs best, demonstrating the most substantial gains in predictive accuracy and minimal error rates. This approach effectively addresses training limitations with limited data by utilizing learned representations from earlier stages, enhancing model performance across all tested architectures.

Furthermore, as shown in Fig. 14, the R^2 comparison between direct training and transfer learning for all models demonstrates significant performance improvements when applying transfer learning with pre-trained models from Stage 1. The FFNN model's R^2 value improved from approximately 0.23 with direct training to about 0.92 with transfer learning. Similarly, the.

CNN model saw an improvement from around 0.81 to 0.82. The LSTM model's R^2 increased from about 0.74 to 0.92, while the BiLSTM model's R^2 value rose from roughly 0.47 to 0.93. The GRU model

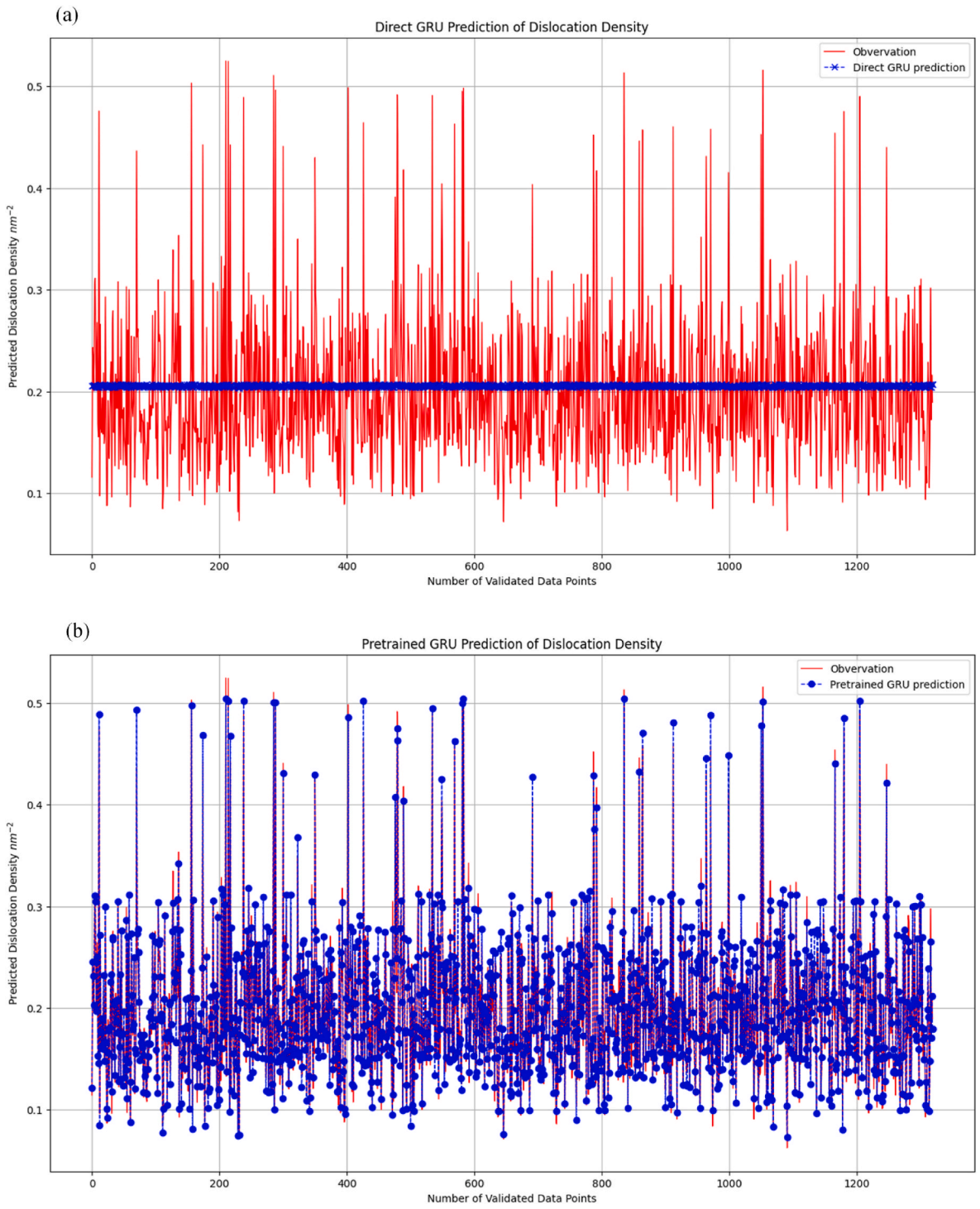

Fig. 15. The dislocation prediction from the GRU model by direct training (a) and transfer learning (b).

exhibited the most significant enhancement, with its R^2 value soaring from about 0.28 to 0.973, marking the best performance among all models. The RNN model also showed improvement, with its R^2 value increasing from around 0.87 to 0.93. These results underscore the effectiveness of transfer learning in enhancing model performance by leveraging pre-trained models from Stage 1, especially when dealing with limited data in Stage 2.

Fig. 15 compares dislocation density predictions using the GRU model trained directly (top) and the pre-trained GRU model (bottom). The top plot illustrates that the GRU model trained directly on the limited dataset failed to accurately predict the dislocation density, as indicated by the significant deviations between the observations (red) and the predictions (blue). In contrast, the bottom plot demonstrates the superior performance of the pre-trained GRU model. The pre-trained model, fine-tuned with the limited data, closely matches the observed dislocation densities, showcasing its enhanced predictive accuracy and ability to generalize better from the pre-trained weights.

Fig. 16(a–b) illustrates the variance in the GRU model's prediction of dislocation values compared to actual observations when trained directly (a) and using a pre-trained model (b). Fig. 16 (a) plot shows that the GRU model trained directly on the limited dataset fails to predict dislocation densities accurately, as evidenced by the significant

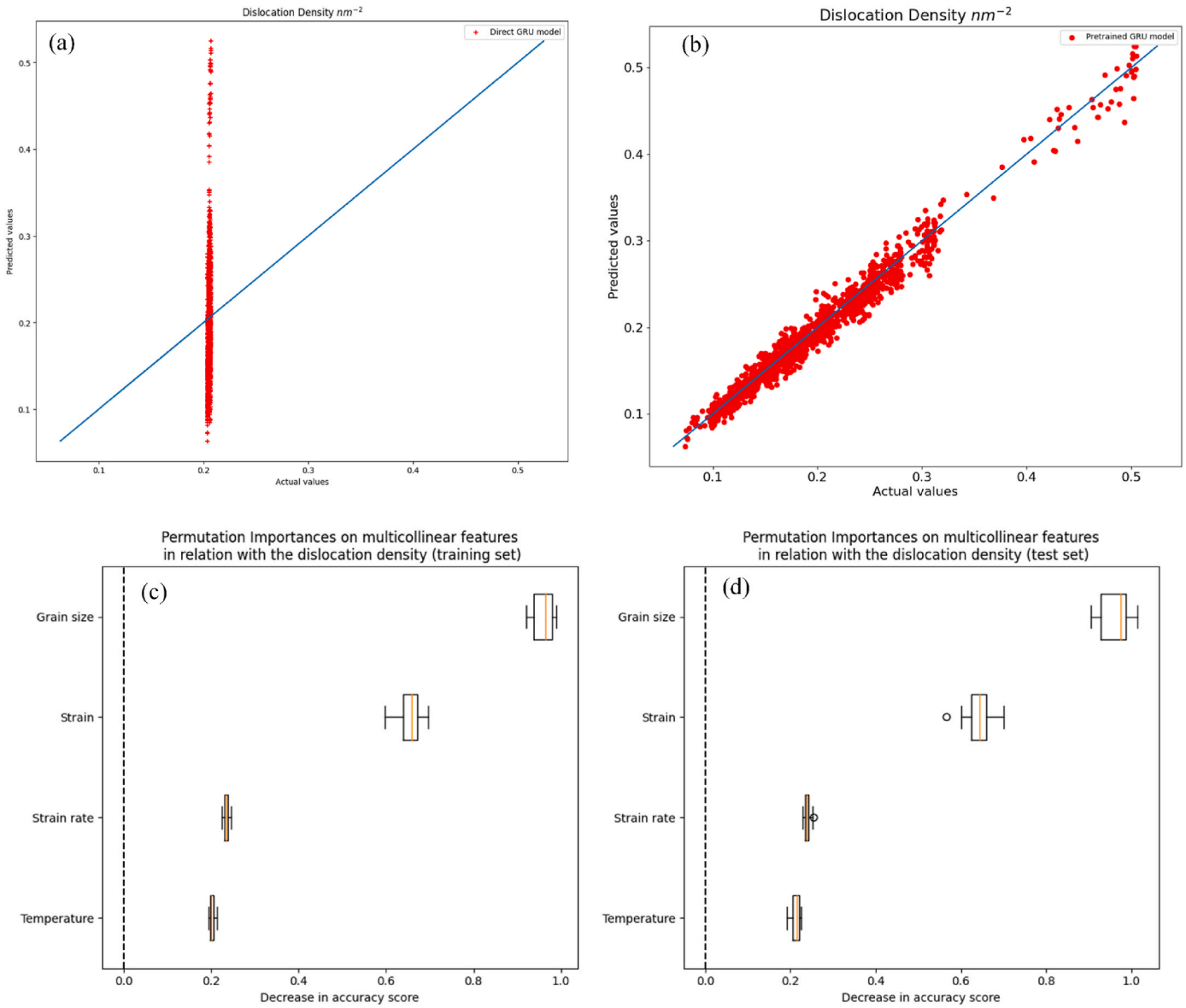

Fig. 16. The variance of the GRU model prediction for dislocation values compared to actual observation by direct training (a) and transfer learning (b). The feature importance regarding dislocation density during training (c) and validation (d).

deviation from the actual values along the vertical axis, indicating poor correlation. In contrast, the right plot demonstrates the superior performance of the pre-trained GRU model, where the predicted values closely follow the actual values along the diagonal line. This close alignment signifies a strong correlation and accurate prediction of dislocation densities, highlighting the effectiveness of using a pre-trained model to improve prediction accuracy. Consequently, Figs. 15 and 16(a–b), along with the R^2 comparison chart Fig. 14, highlight the significant benefits of transfer learning using a pre-trained model over direct training, particularly for the GRU model. This comprehensive analysis underscores the effectiveness of transfer learning in enhancing model performance, mainly when data is limited. The GRU model stands out, demonstrating the most substantial improvement and superior performance, making it the most effective model for predicting dislocation densities in this study.

Fig. 16(c–d) presents the permutation importance of multicollinear features with the dislocation density for the training set (c) and the test set (d). The analysis identifies the most and least important features for predicting dislocation density. The most important feature is grain size, which shows the highest decrease in accuracy score when permuted, indicating its significant impact on the model's predictions. The least important feature is temperature, as it exhibits the smallest decrease in accuracy score, suggesting a minimal effect on the prediction of dislocation density. The consistency of feature importance between the training and validation sets highlights the robustness of the model. Both sets show similar importance rankings for the features, reinforcing the model's ability to understand and capture the relationship between each input feature and the output dislocation density. This consistency suggests that the model generalizes well from training to validation, maintaining reliable performance and interpretability across different data sets.

Fig. 17 presents the partial dependence plots of dislocation values for different input features: strain, temperature, grain size, and strain rate. These plots provide detailed insights into the relationship between each feature and the predicted dislocation values, indicating whether these relationships are linear or non-linear. The top-left plot shows the partial dependence of dislocation values on strain. The relationship is non-linear, with dislocation values increasing with strain up to approximately 0.4, after which the values plateau and slightly decrease. This indicates that strain significantly impacts dislocation values up to a

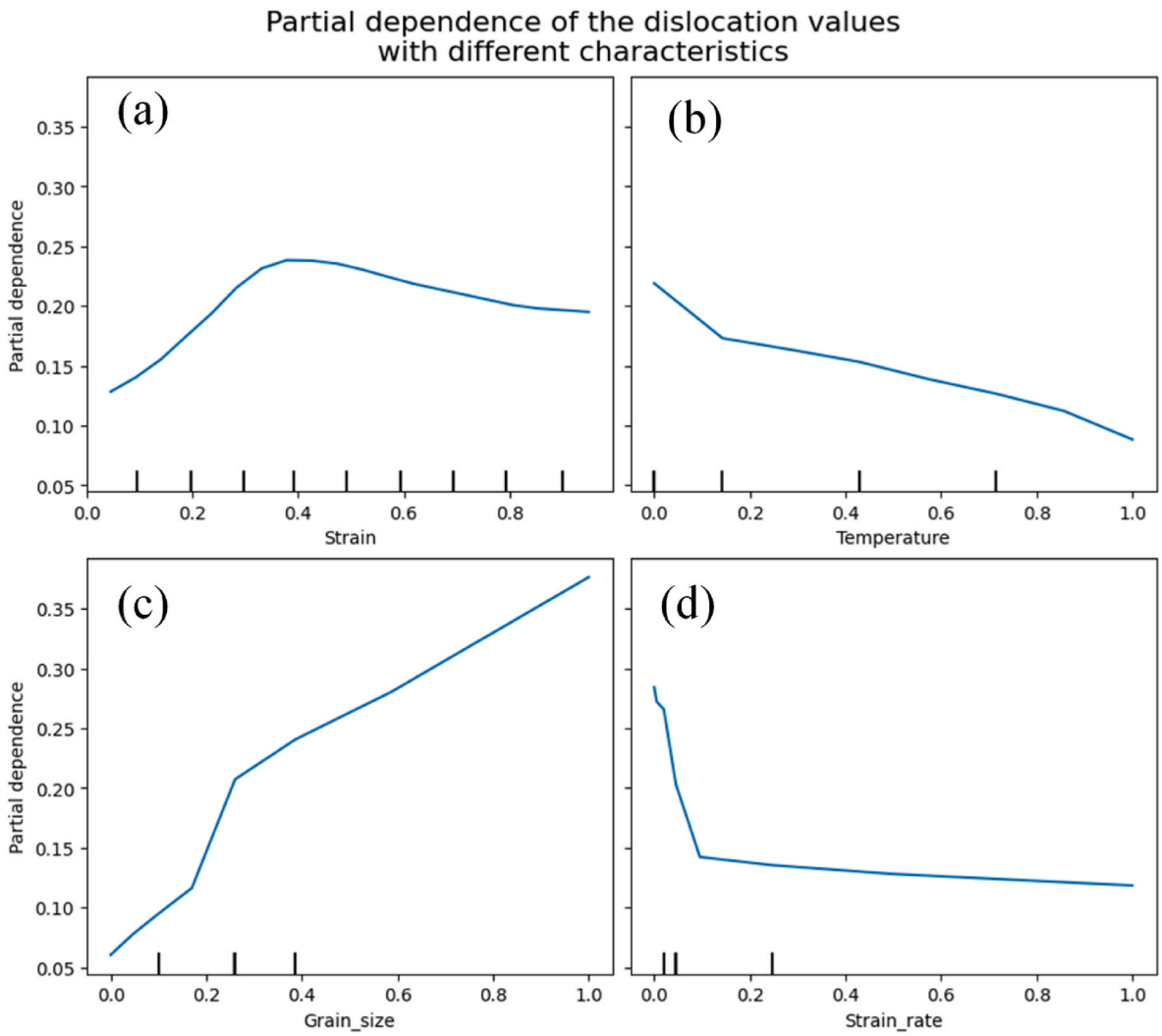

Fig. 17. The partial dependence between the dislocation values and a set of features of interest.

certain point, beyond which its effect stabilizes. The top-right plot depicts the partial dependence on temperature. This relationship is predominantly linear, with dislocation values decreasing steadily as temperature increases. This suggests higher temperatures are associated with lower dislocation densities, indicating a linear inverse correlation. The bottom-left plot illustrates the partial dependence on grain size, showing a solid nonlinear relationship. Dislocation values increase sharply with grain size initially and continue to rise steadily, indicating that larger grain sizes are associated with higher dislocation densities. This strong positive correlation highlights the significant impact of grain size on dislocation values. The bottom-right plot shows the partial dependence on strain rate. The relationship is non-linear, with a steep initial decline in dislocation values as the strain rate increases, followed by a more gradual decrease. This indicates that higher strain rates initially lead to lower dislocation densities, but the effect diminishes at higher strain rates. These partial dependence plots reveal that the relationships between input features and dislocation values are a mix of linear and non-linear correlations. Strain and strain rate exhibit non-linear relationships, while temperature shows a linear inverse correlation. Grain size has a solid non-linear positive correlation with dislocation values. These detailed insights help us understand how each input feature influences the output, highlighting the complex nature of the

Table 7
A comparative analysis of the findings from this study and previous research.

Materials	Strain rate (s^{-1})	Temperature (K)	Strain (%)	Strain (Gpa)	Predictive model	Method	Reference
AlCoCrCuFeNi	10^8 - 2×10^{10}	300–1000	0.2	3.12–5.75	LR, SVR, GRB, FFNN, CNN, LSTM, BiLSTM, GRU, RNN	MD and ML	This study
HEA	–	–	–	–	ANN, SVM, GA	MD	Durodola et al. [30]
FeCoNiCrCu	–	300–1273	–	–	GMM, MCMC	ML	Rao et al. [32]
HEA	–	1500–2300	–	0.32–1.62	NN, ANN, SVM, GP, GAN, CART	MD, ML	Liu et al. [37]
AlCoCrCuFeNi	10^{-3}	300–1473	0.27	1.482–1.795	–	Exp	Deng et al. [45]
CuFeNiCrCo	10^7–10^9	300–3000	0.1–0.24	7.66–15.14	DNN, SVM, KELM, ELM	MD, ML	Zhang et al. [46]
CoCrFeNi	5×10^{-5} – 6.5×10^3	200–1473	0.33	–	–	MD and Exp	Cao et al. [60]

interactions in the model.

Research on these alloy systems has demonstrated a range of mechanical behavior under tension testing, influenced by variables such as grain size, temperature, and strain rate, facilitated by machine learning techniques. This study offers an in-depth analysis of high-entropy alloys, distinguishing itself by incorporating tensile deformation models to predict stress and dislocation density through a novel combination of molecular dynamics simulation and machine learning. The tensile strength results corroborate those reported by Li et al. [14], and while temperature and strain rate measurements exceed those documented by Deng et al. [55], they are consistent with Zhang et al. [57]. The comparison of mechanical behavior across various studies, summarized in Table 7, supports the study's conclusions and reinforces its alignment with existing research. These findings are anticipated to provide valuable insights for future studies on AlCoCrCuFeNi high-entropy alloys.

4. Conclusions

The mechanical behavior and deformation mechanism of AlCoCrCuFeNi high-entropy alloy samples are explored by integrating molecular dynamics simulations and machine learning assistance. This investigation scrutinizes the impact of temperature variations, tension strain rates, and grain size on the mechanical properties. Elevated temperatures induce softening in the AlCoCrCuFeNi HEA sample, leading to a decrease in interatomic connectivity. Consequently, Young's modulus, average flow stress, and ultimate stress exhibit reductions. Moreover, the increase in temperature expands the amorphization zone, shortening the overall dislocation density. The proposed ML framework, particularly the GRU-based model enhanced through transfer learning, not only demonstrates high predictive accuracy for stress and dislocation density in AlCoCrCuFeNi HEAs but also establishes a generalizable pipeline for accelerating mechanical property prediction in complex alloys. Given the same set of input features derived from mechanical characteristics, the ML model effectively learns underlying correlations, and transfer learning further enhances its adaptability to predict new target properties without requiring retraining from scratch. Consequently, by significantly reducing simulation time, the framework enables rapid screening of candidate compositions and processing conditions in materials discovery workflows. Compared to prior studies that rely solely on physics-based modeling or empirical fits, our approach integrates molecular dynamics and deep learning to capture nonlinear, multivariate dependencies with high fidelity. Furthermore, while previous research [17,57,87,88] has applied ML to similar problems, our dual-stage, transfer-learning-enhanced model uniquely bridges atomic-level simulations and predictive analytics, offering a scalable solution for high-throughput computational materials design.

This study presents a comprehensive workflow that leverages transfer learning by utilizing pre-trained models from stress prediction (Stage 1) to enhance the prediction of dislocation densities (Stage 2). The workflow begins with obtaining detailed MD simulation data to train models for stress prediction. The pre-trained models are then fine-tuned with additional data to predict dislocation densities, effectively reducing the total simulation time.

The benefits of this workflow are evident in the significant improvement of evaluation metrics for all machine learning models. The comparison of direct training and transfer learning shows a substantial enhancement in R^2 values, underscoring the effectiveness of transfer learning in capturing the complex relationships in the data. This approach improves predictive accuracy and ensures robust model performance with limited data.

Among all the machine learning models evaluated, the GRU model stands out as the best performer in both stages, demonstrating superior predictive capabilities for stress and dislocation densities. The GRU model consistently achieved the highest R^2 values and lowest errors, making it the most effective model in this study.

Furthermore, the study provides a detailed understanding of the importance of features and relationships between input features and outputs (stress and dislocation). Using the importance of permutation features, we identified grain size as the most critical feature and temperature as the least important. Partial dependence analysis further revealed the nature of these relationships, highlighting both linear and non-linear correlations between the features and the outputs.

In summary, this study significantly improves dislocation prediction by reducing MD simulation time by fourfold (from 118 days to 29 days), thus saving time and cost. It demonstrates the robustness of the GRU model for accurate predictions and enhances interpretability through detailed feature analysis. This approach offers a promising framework for efficiently predicting mechanical properties in high-entropy alloys and other complex materials.

CRediT authorship contribution statement

Hoang-Giang Nguyen: Writing – review & editing, Writing – original draft, Visualization, Validation, Software, Methodology, Investigation, Formal analysis, Data curation, Conceptualization. **Sheng-Joue Young:** Supervision, Software, Resources, Project administration, Funding acquisition. **Thanh-Dung Le:** Writing – review & editing, Writing – original draft, Visualization, Validation, Software, Formal analysis, Data curation, Conceptualization. **Symeon Chatzinotas:** Supervision, Software, Methodology, Funding acquisition. **Te-Hua Fang:** Writing – review & editing, Supervision, Software, Resources, Project administration, Methodology, Formal analysis.

Declaration of competing interest

The authors declare the following financial interests/personal relationships which may be considered as potential competing interests: Te-Hua Fang reports financial support was provided by National Kaohsiung University of Science and Technology. Sheng-Joue Young reports financial support was provided by National United University. Hoang-Giang Nguyen reports financial support was provided by Kien Giang University. If there are other authors, they declare that they have no known competing financial interests or personal relationships that could have appeared to influence the work reported in this paper.

Acknowledgments

The authors acknowledge the support by the National Science and Technology Council, Taiwan, under grant numbers NSTC 113-2221-E-992-067-MY3, NSTC 113-2811-E239-002, NSTC 114-2221-E-992 -029 -MY3, NSTC 114-2221-E-992 -030 -MY3, the Industry Cooperation Project No. 113A00262, and the Ministry of Education and Training, Vietnam, under grant number B2026-TKG-01.

Data availability

The authors do not have permission to share data.

References

[1] P. Pandey, N. Khatavkar, S. Kumar, H. Oh, A. Godha, S.K. Makineni, K. Chattopadhyay, Plastic deformation and strengthening mechanisms in CoNiCrFe high entropy alloys: the role of lattice site occupancy, Int. J. Plast. (2024) 104145.

[2] K. Itoh, Y. Yoshioka, E.R. Barney, A.C. Hannon, Free volume distribution and structural inhomogeneity in Ni50V50 amorphous alloy, J. Alloys Compd. 770 (2019) 350–355.

[3] J.X. Fu, et al., The tensile properties and serrated flow behavior of a thermomechanically treated CoCrFeNiMn high-entropy alloy, Mater. Sci. Eng., A 690 (2017) 418–426.

[4] Z. Sun, M. Roscher, M.C. Paolantonio, V. Soh, C. Liu, S.P. Tsai, E.A. Jägle, Additive manufacturing of sustainable and heat-resistant Al-Fe-Mo-Si-Zr alloys, J. Alloys Compd. (2024) 177118.

[5] R. Gao, X.X. Ye, S. Yan, Y. Lu, L. Jiang, Z. Li, X. Zhou, Effects of tungsten content on the high-temperature oxidation behavior of Ni-xW-6Cr alloys, Corros. Sci. 149 (2019) 87–99.
[6] H. Chen, A. Kauffmann, B. Gorr, D. Schliephake, C. Seemüller, J.N. Wagner, M. Heilmaier, Microstructure and mechanical properties at elevated temperatures of a new Al-containing refractory high-entropy alloy Nb-Mo-Cr-Ti-Al, J. Alloys Compd. 661 (2016) 206–215.
[7] H. Prasad, S. Singh, B.B. Panigrahi, Mechanical activated synthesis of alumina dispersed FeNiCoCrAlMn high entropy alloy, J. Alloys Compd. 692 (2017) 720–726.
[8] W. Li, D. Xie, D. Li, Y. Zhang, Y. Gao, P.K. Liaw, Mechanical behavior of high-entropy alloys, Prog. Mater. Sci. 118 (2021) 100777.
[9] M.H. Tsai, Three strategies for the design of advanced high-entropy alloys, Entropy 18 (7) (2016) 252.
[10] P.A. Ibrahim, İ. Özkul, C.A. Canbay, An overview of high-entropy alloys, Emergent Materials 5 (6) (2022) 1779–1796.
[11] W. Li, P. Liu, P.K. Liaw, Microstructures and properties of high-entropy alloy films and coatings: a review, Materials Research Letters 6 (4) (2018) 199–229.
[12] Z. Li, Y. Gu, C. Wang, M. Pan, H. Zhang, Z. Wu, H. Xu, Microstructure and magnetic properties of the FeCoNi (CuAl) 0.8 Ga0. 06 high-entropy alloy during the phase transition, J. Alloys Compd. 779 (2019) 293–300.
[13] J.Y. Chen, H.G. Nguyen, M.H. Lin, T.H. Fang, Mechanical and electrochemical characterization of CuAlNi alloys, Curr. Appl. Phys. 69 (2025) 8–20.
[14] W. Li, P.K. Liaw, Y. Gao, Fracture resistance of high entropy alloys: a review, Intermetallics 99 (2018) 69–83.
[15] W. Wu, Z. Liu, X. Li, C. Du, Z. Cui, Influence of different heat-affected zone microstructures on the stress corrosion behavior and mechanism of high-strength low-alloy steel in a sulfurated marine atmosphere, Mater. Sci. Eng., A 759 (2019) 124–141.
[16] H.G. Nguyen, S.J. Young, T.D. Le, T.N. Vu, T.H. Fang, Bauschinger effect on high entropy alloy under cyclic deformation, Intermetallics 183 (2025) 108830.
[17] H.G. Nguyen, T.D. Le, H.G. Nguyen, T.H. Fang, Mechanical properties of AlCoCrCuFeNi high-entropy alloys using molecular dynamics and machine learning, Mater. Sci. Eng. R Rep. 160 (2024) 100833.
[18] H.G. Nguyen, T.H. Fang, Mechanics of AlCuNiTi alloy orthogonal micro-cutting, Model. Simulat. Mater. Sci. Eng. 31 (8) (2023) 085016.
[19] C.H. Wang, K.C. Chao, T.H. Fang, I. Stachiv, S.F. Hsieh, Investigations of the mechanical properties of nanoimprinted amorphous Ni–Zr alloys utilizing the molecular dynamics simulation, J. Alloys Compd. 659 (2016) 224–231.
[20] Y. Gao, H.M. Urbassek, Scratching of nanocrystalline metals: a molecular dynamics study of Fe, Appl. Surf. Sci. 389 (2016) 688–695.
[21] S. Qin, L. Zhu, Surface and subsurface damage of laser assisted grinding CrCoNi medium-entropy alloy at atomic/nano scale, Tribol. Int. 191 (2024) 109121.
[22] J. Li, Q. Fang, B. Liu, Y. Liu, Y. Liu, Mechanical behaviors of AlCrFeCuNi high-entropy alloys under uniaxial tension via molecular dynamics simulation, RSC Adv. 6 (80) (2016) 76409–76419.
[23] D.Q. Doan, T.H. Fang, T.H. Chen, Influences of grain size and temperature on tribological characteristics of CuAlNi alloys under nanoindentation and nanoscratch, Int. J. Mech. Sci. 185 (2020) 105865.
[24] H.G. Nguyen, M.J. Wu, T.H. Fang, Study on copper-to-copper bonding of three-dimensional integrated circuits using the quasicontinuum method, Phys. Scri. 99 (6) (2024) 065114.
[25] A.T. AlMotasem, J. Bergström, A. Gåård, P. Krakhmalev, L.J. Holleboom, Tool microstructure impact on the wear behavior of ferrite iron during nanoscratching: an atomic level simulation, Wear 370 (2017) 39–45.
[26] S.Z. Chavoshi, X. Luo, Molecular dynamics simulation study of deformation mechanisms in 3C–SiC during nanometric cutting at elevated temperatures, Mater. Sci. Eng., A 654 (2016) 400–417.
[27] G. Wang, G. Zhao, J. Song, Q. Ding, Study on tribological properties of TMDs-coated copper from the nanoscale, Mater. Today Commun. 31 (2022) 103815.
[28] R. Chang, W. Fang, H. Yu, X. Bai, X. Zhang, B. Liu, F. Yin, Heterogeneous banded precipitation of (CoCrNi) 93Mo7 medium entropy alloys towards strength–ductility synergy utilizing compositional inhomogeneity, Scr. Mater. 172 (2019) 144–148.
[29] J. Qiu, C. Zhou, B. Liu, Y. Liu, H. Li, X. Liang, X. Zan, Precipitation behavior of Ti-45Al-3Fe-2Mo-0.5 C intermetallics after creep tests at 750° C, Mater. Char. 155 (2019) 109825.
[30] J.F. Durodola, Machine learning for design, phase transformation and mechanical properties of alloys, Prog. Mater. Sci. 123 (2022) 100797.
[31] H.G. Nguyen, T.H. Fang, Material properties and machining behavior of AlCuNiTiZr with molecular dynamic simulation, Model. Simulat. Mater. Sci. Eng. 33 (5) (2025) 055015.
[32] Z. Rao, P.Y. Tung, R. Xie, Y. Wei, H. Zhang, A. Ferrari, D. Raabe, Machine learning–enabled high-entropy alloy discovery, Science 378 (6615) (2022) 78–85.
[33] B. Xin, A. Zhang, J. Han, B. Su, J. Meng, Tuning composition and microstructure by doping Ti and C for enhancing mechanical property and wear resistance of Al0. 2Co1. 5CrFeNi1. 5Ti0. 5 high entropy alloy matrix composites, J. Alloys Compd. 836 (2020) 155273.
[34] R. Mayahi, An investigation concerning generalized stacking fault behavior of AlCoxCrFeNi (0.25≤ x≤ 2) high entropy alloys: insights from first-principles study, J. Alloys Compd. 818 (2020) 152928.
[35] E.P. George, D. Raabe, R.O. Ritchie, High-entropy alloys, Nat. Rev. Mater. 4 (8) (2019) 515–534.
[36] H. Jiang, D. Qiao, W. Jiao, K. Han, L. Yiping, P.K. Liaw, Tensile deformation behavior and mechanical properties of a bulk cast Al0. 9CoFeNi2 eutectic high-entropy alloy, J. Mater. Sci. Technol. 61 (2021) 119–124.
[37] X. Liu, J. Zhang, Z. Pei, Machine learning for high-entropy alloys: progress, challenges and opportunities, Prog. Mater. Sci. 131 (2023) 101018.
[38] J.B. Ri, Z. Wen, Q. Jiang, A criterion for the glass-forming ability of binary bulk metallic glasses, J. Non-Cryst. Solids 471 (2017) 264–267.
[39] L. Meshi, Y. Linden, A. Munitz, S. Salhov, M. Pinkas, Retardation of the σ phase formation in the AlCoCrFeNi multi-component alloy, Mater. Char. 148 (2019) 171–177.
[40] J. Sun, H. Li, Y. Chen, X. An, Bidirectional phase transformations in multi-principal element alloys: mechanisms, physics, and mechanical property implications, Adv. Sci. (2024) 2407283.
[41] C. Oses, C. Toher, S. Curtarolo, High-entropy ceramics, Nat. Rev. Mater. 5 (4) (2020) 295–309.
[42] Y. Tong, J.C. Qiao, C. Zhang, J.M. Pelletier, Y. Yao, Mechanical properties of Ti16. 7Zr16. 7Hf16. 7Cu16. 7Ni16. 7Be16. 7 high-entropy bulk metallic glass, J. Non-Cryst. Solids 452 (2016) 57–61.
[43] C. Ni, Y. Shi, J. Liu, G. Huang, Characterization of Al0. 5FeCu0. 7NiCoCr high-entropy alloy coating on aluminum alloy by laser cladding, Opt Laser. Technol. 105 (2018) 257–263.
[44] J. Su, X. Wu, D. Raabe, Z. Li, Deformation-driven bidirectional transformation promotes bulk nanostructure formation in a metastable interstitial high entropy alloy, Acta Mater. 167 (2019) 23–39.
[45] N. Deng, J. Wang, J. Wang, Y. He, E. Beaugnon, J. Li, Effect of high magnetic field assisted heat treatment on microstructure and properties of AlCoCrCuFeNi high-entropy alloy, Mater. Lett. 303 (2021) 130540.
[46] L. Zhang, K. Qian, B.W. Schuller, Y. Shibuta, Prediction on mechanical properties of non-equiatomic high-entropy alloy by atomistic simulation and machine learning, Metals 11 (6) (2021) 922.
[47] Z. Li, S. Zhao, R.O. Ritchie, M.A. Meyers, Mechanical properties of high-entropy alloys with emphasis on face-centered cubic alloys, Prog. Mater. Sci. 102 (2019) 296–345.
[48] K. Tang, Y.K. Wu, R. Wei, L.B. Chen, S. Lu, Y.L. Qi, J. Sun, Achieving superior cryogenic tensile properties in a Ti-doped (Fe40Mn40Co10Cr10) 96.7 C3. 3 high-entropy alloy by recovering deformation twinning, Mater. Sci. Eng., A 808 (2021) 140927.
[49] T.N. Yang, C. Lu, G. Velisa, K. Jin, P. Xiu, Y. Zhang, L. Wang, Influence of irradiation temperature on void swelling in NiCoFeCrMn and NiCoFeCrPd, Scr. Mater. 158 (2019) 57–61.
[50] N. Karathanasopoulos, P. Hadjidoukas, Deep learning based automated fracture identification in material characterization experiments, Adv. Eng. Inform. 60 (2024) 102402.
[51] Y. Chew, G.J. Bi, Z.G. Zhu, F.L. Ng, F. Weng, S.B. Liu, B.Y. Lee, Microstructure and enhanced strength of laser aided additive manufactured CoCrFeNiMn high entropy alloy, Mater. Sci. Eng., A 744 (2019) 137–144.
[52] C. Lee, F. Maresca, R. Feng, Y. Chou, T. Ungar, M. Widom, W.A. Curtin, Strength can be controlled by edge dislocations in refractory high-entropy alloys, Nat. Commun. 12 (1) (2021) 5474.
[53] E.J. Pickering, H.J. Stone, N.G. Jones, Fine-scale precipitation in the high-entropy alloy Al0. 5CrFeCoNiCu, Mater. Sci. Eng., A 645 (2015) 65–71;
(a) X. Xian, L. Lin, Z. Zhong, C. Zhang, C. Chen, K. Song, Y. Wu, Precipitation and its strengthening of Cu-rich phase in CrMnFeCoNiCux high-entropy alloys, Mater. Sci. Eng., A 713 (2018) 134–140.
[54] D.Q. Zhao, S.P. Pan, Y. Zhang, P.K. Liaw, J.W. Qiao, Structure prediction in high-entropy alloys with machine learning, Appl. Phys. Lett. 118 (23) (2021).
[55] D. Zhao, X. Jin, J. Qiao, Y. Zhang, P.K. Liaw, Machine-learning-assisted modeling of alloy ordering phenomena at the electronic scale through electronegativity, Appl. Phys. Lett. 124 (11) (2024).
[56] D. Zhao, J. Qiao, Space group prediction of complex alloy systems by product-based neural networks, Intermetallics 175 (2024) 108489.
[57] H.G. Nguyen, S.J. Young, T.D. Le, C.N. Nguyen, L.B. Do, T.N. Nguyen, T.H. Fang, Molecular dynamics simulation and machine learning to predict mechanical behavior of Cu/Zr multilayer nanofilms under tension-compression, J. Non-Cryst. Solids 666 (2025) 123682.
[58] K. Jiang, Q. Zhang, J. Li, X. Li, F. Zhao, B. Hou, T. Suo, Abnormal hardening and amorphization in an FCC high entropy alloy under extreme uniaxial tension, Int. J. Plast. 159 (2022) 103463.
[59] Q. Zhang, R. Huang, J. Jiang, T. Cao, Y. Zeng, J. Li, X. Li, Size effects and plastic deformation mechanisms in single-crystalline CoCrFeNi micro/nanopillars, J. Mech. Phys. Solid. 162 (2022) 104853.
[60] T. Cao, Q. Zhang, L. Wang, L. Wang, Y. Xiao, J. Yao, X. Li, Dynamic deformation behaviors and mechanisms of CoCrFeNi high-entropy alloys, Acta Mater. 260 (2023) 119343.
[61] M.P. Allen, Introduction to molecular dynamics simulation, Computational soft matter: from synthetic polymers to proteins 23 (1) (2004) 1–28.
[62] L.A. Segel, G.H. Handelman, Mathematics Applied to Continuum Mechanics, Society for Industrial and Applied Mathematics, 2007.
[63] R. Komanduri, L.M. Raff, A review on the molecular dynamics simulation of machining at the atomic scale, Proc. IME B J. Eng. Manufact. 215 (12) (2001) 1639–1672.
[64] A. Sharma, P. Ranjan, R. Balasubramaniam, Investigation of effect of uncut chip thickness to edge radius ratio on nanoscale cutting behavior of single crystal copper: MD simulation approach, Journal of Micromanufacturing 4 (1) (2021) 6–17.

[65] S. Plimpton, Fast parallel algorithms for short-range molecular dynamics, J. Comput. Phys. 117 (1) (1995) 1–19.
[66] S.J. Plimpton, C. Knight, Rendezvous algorithms for large-scale modeling and simulation, J. Parallel Distr. Comput. 147 (2021) 184–195.
[67] L. Verlet, Computer" experiments" on classical fluids. I. Thermodynamical properties of Lennard-Jones molecules, Phys. Rev. 159 (1) (1967) 98.
[68] L. Verlet, Computer experiments on classical fluids. ii. equilibrium correlation functions, Phys. Rev. 165 (1968) 201–214.
[69] J.W. Eastwood, W. Arter, N.J. Brealey, R.W. Hockney, Body-fitted electromagnetic PIC software for use on parallel computers, Comput. Phys. Commun. 87 (1–2) (1995) 155–178.
[70] W.C. Swope, H.C. Andersen, P.H. Berens, K.R. Wilson, A computer simulation method for the calculation of equilibrium constants for the formation of physical clusters of molecules: application to small water clusters, J. Chem. Phys. 76 (1) (1982) 637–649.
[71] H.L. Jang, J.H. Kim, S.H. Kang, S. Cho, Y. Park, Optimal mass distribution in carbon nanotubes for extreme thermal conductivity: analytical manipulation of isotope effects, Comput. Mater. Sci. 150 (2018) 273–282.
[72] A. Sharma, S.A. Deshmukh, P.K. Liaw, G. Balasubramanian, Crystallization kinetics in AlxCrCoFeNi (0≤ x≤ 40) high-entropy alloys, Scr. Mater. 141 (2017) 54–57.
[73] E. Della Valle, P. Marracino, S. Setti, R. Cadossi, M. Liberti, F. Apollonio, Magnetic molecular dynamics simulations with Velocity Verlet algorithm, in: 2017 XXXIInd General Assembly and Scientific Symposium of the International Union of Radio Science (URSI GASS), IEEE, 2017, August, pp. 1–4.
[74] J. Jung, C. Kobayashi, Y. Sugita, Optimal temperature evaluation in molecular dynamics simulations with a large time step, J. Chem. Theor. Comput. 15 (1) (2018) 84–94.
[75] C. Massobrio, I.A. Essomba, M. Boero, C. Diarra, M. Guerboub, K. Ishisone, S. D. Wansi Wendji, On the actual difference between the Nosé and the nosé–hoover thermostats: a critical review of canonical temperature control by molecular dynamics, Phys. Status Solidi 261 (1) (2024) 2300209.
[76] Z. Li, S. Xiong, C. Sievers, Y. Hu, Z. Fan, N. Wei, T. Ala-Nissila, Influence of thermostatting on nonequilibrium molecular dynamics simulations of heat conduction in solids, J. Chem. Phys. 151 (23) (2019).
[77] M.S. Nitol, M.J. Echeverria, K. Dang, M.I. Baskes, S.J. Fensin, New modified embedded-atom method interatomic potential to understand deformation behavior in VNbTaTiZr refractory high entropy alloy, Comput. Mater. Sci. 237 (2024) 112886.
[78] D. Utt, A. Stukowski, K. Albe, Grain boundary structure and mobility in high-entropy alloys: a comparative molecular dynamics study on a Σ11 symmetrical tilt grain boundary in face-centered cubic CuNiCoFe, Acta Mater. 186 (2020) 11–19.
[79] Y. Zhang, K. Ding, S. Stangebye, D. Chen, J. Kacher, O. Pierron, T. Zhu, Atomistic modeling of surface and grain boundary dislocation nucleation in FCC metals, Acta Mater. 237 (2022) 118155.
[80] M. He, C. Wu, M.V. Shugaev, G.D. Samolyuk, L.V. Zhigilei, Computational study of short-pulse laser-induced generation of crystal defects in Ni-based single-phase binary solid–solution alloys, J. Phys. Chem. C 123 (4) (2019) 2202–2215.
[81] S. Zhang, Y. Xu, X. Liu, S.N. Luo, Competing roles of interfaces and matrix grain size in the deformation and failure of polycrystalline Cu–graphene nanolayered composites under shear loading, Phys. Chem. Chem. Phys. 20 (36) (2018) 23694–23701.
[82] T.N. Vu, V.T. Pham, T.H. Fang, Deformation mechanisms and mechanical properties of nanocrystalline CuxNi100− x alloys during indentation using molecular dynamics, Mater. Today Commun. 33 (2022) 104282.
[83] T.N. Vu, V.T. Pham, T.H. Fang, Maintain sort order of grain boundary to investigate the deformation mechanism of CoCuFeNiPd high–entropy alloys, Curr. Appl. Phys. 59 (2024) 46–59.
[84] A.V. Pham, T.H. Fang, A.S. Tran, T.H. Chen, Structural and mechanical characterization of sputtered CuxNi100-x thin film using molecular dynamics, J. Phys. Chem. Solid. 147 (2020) 109663.
[85] J.D. Honeycutt, H.C. Andersen, Molecular dynamics study of melting and freezing of small Lennard-Jones clusters, J. Phys. Chem. 91 (19) (1987) 4950–4963.
[86] Y. Qi, H. Xu, T. He, M. Wang, M. Feng, Atomistic simulation of deformation behaviors polycrystalline CoCrFeMnNi high-entropy alloy under uniaxial loading, Int. J. Refract. Metals Hard Mater. 95 (2021) 105415.
[87] T.D. Le, R. Noumeir, H.L. Quach, J.H. Kim, J.H. Kim, H.M. Kim, Critical temperature prediction for a superconductor: a variational bayesian neural network approach, IEEE Trans. Appl. Supercond. 30 (4) (2020) 1–5.
[88] J.F. Masson, J.S. Biggins, E. Ringe, Machine learning for nanoplasmonics, Nat. Nanotechnol. 18 (2) (2023) 111–123.
[89] D.C. Montgomery, E.A. Peck, G.G. Vining, Introduction to Linear Regression Analysis, John Wiley & Sons, 2021.
[90] F. Zhang, L.J. O'Donnell, Support vector regression, in: Machine Learning, Academic Press, 2020, pp. 123–140.
[91] J.H. Friedman, Greedy function approximation: a gradient boosting machine, Ann. Stat. (2001) 1189–1232.
[92] Y. LeCun, Y. Bengio, G. Hinton, Deep learning, Nature 521 (7553) (2015) 436–444.
[93] Z. Li, F. Liu, W. Yang, S. Peng, J. Zhou, A survey of convolutional neural networks: analysis, applications, and prospects, IEEE Transact. Neural Networks Learn. Syst. 33 (12) (2021) 6999–7019.
[94] Y. Yu, X. Si, C. Hu, J. Zhang, A review of recurrent neural networks: LSTM cells and network architectures, Neural Comput. 31 (7) (2019) 1235–1270.
[95] T. Peng, C. Zhang, J. Zhou, M.S. Nazir, An integrated framework of Bi-directional long-short term memory (BiLSTM) based on sine cosine algorithm for hourly solar radiation forecasting, Energy 221 (2021) 119887.
[96] M. Ravanelli, P. Brakel, M. Omologo, Y. Bengio, Light gated recurrent units for speech recognition, IEEE Transactions on Emerging Topics in Computational Intelligence 2 (2) (2018) 92–102.
[97] S. Grossberg, Recurrent neural networks, Scholarpedia 8 (2) (2013) 1888.
[98] T. Hastie, R. Tibshirani, J.H. Friedman, J.H. Friedman, The Elements of Statistical Learning: Data Mining, Inference, and Prediction, vol. 2, Springer, New York, 2009, pp. 1–758.
[99] W.J. Murdoch, C. Singh, K. Kumbier, R. Abbasi-Asl, B. Yu, Definitions, methods, and applications in interpretable machine learning, Proc. Natl. Acad. Sci. 116 (44) (2019) 22071–22080.
[100] V.T. Pham, T.N. Vu, T.H. Fang, D.B. Luu, V.T. Hoang, N.H. Tran, Q.B. Tao, Effects of microstructure and vibration parameters on mechanical properties of nanoimprinted FeNiCrCoCu high-entropy alloys, Phys. B Condens. Matter 665 (2023) 415028.
[101] J. Jiang, W. Sun, N. Luo, Molecular dynamics study of microscopic deformation mechanism and tensile properties in AlxCoCrFeNi amorphous high-entropy alloys, Mater. Today Commun. 31 (2022) 103861.
[102] T.N. Vu, V.T. Pham, T.H. Fang, Effects of structure and strain rate on deformation mechanism of twin lamellar Al0. 3CoCrFeNi alloys, J. Alloys Compd. 954 (2023) 170174.
[103] T. Fu, X. Peng, C. Huang, S. Weng, Y. Zhao, Z. Wang, N. Hu, Strain rate dependence of tension and compression behavior in nano-polycrystalline vanadium nitride, Ceram. Int. 43 (15) (2017) 11635–11641.
[104] V.T. Pham, T.H. Fang, Understanding porosity and temperature induced variabilities in interface, mechanical characteristics and thermal conductivity of borophene membranes, Sci. Rep. 11 (1) (2021) 12123.
[105] W. Zhou, X. Ren, Y. Yang, Z. Tong, L. Chen, Dislocation behavior in nickel and iron during laser shock-induced plastic deformation, Int. J. Adv. Des. Manuf. Technol. 108 (2020) 1073–1083.
[106] Y. Wang, B. Hu, X. Liu, H. Zhang, H. Zhang, Z. Guan, H. Luo, Influence of annealing temperature on both mechanical and damping properties of Nb-alloyed high Mn steel, Acta Metall. Sin. 57 (12) (2021) 1588–1594.
[107] D. Wen, B. Kong, S. Wang, M. Zhang, G. Wang, X. Wang, S. Li, Atomic-scale investigation on fretting wear mechanism of γ phase in a cast Ti-45Al alloy, Appl. Surf. Sci. 565 (2021) 150555.
[108] J. Jiang, W. Sun, N. Luo, Atomic insights into effects of temperature and grain diameter on the micro-deformation mechanism, mechanical properties and sluggish diffusion of nanocrystalline high-entropy alloys, Mater. Today Commun. 33 (2022) 104224.
[109] Dinh-Quan Doan, Te-Hua Fang, Tao-Hsing Chen, Effects of grain and twin boundary on friction and contact characteristics of CuZrAl nanocrystallines, Appl. Surf. Sci. 524 (2020) 146458.
[110] Y. Hu, S. Ding, J. Xu, Y. Zhang, J. Li, W. Wu, R. Xia, Revealing the toughening mechanisms in graphene/tungsten nanocomposites with hierarchical nacre-like structures, Compos. Struct. 321 (2023) 117322.
[111] S. Chen, Z.H. Aitken, Z. Wu, Z. Yu, R. Banerjee, Y.W. Zhang, Hall-Petch and inverse Hall-Petch relations in high-entropy CoNiFeAlxCu1-x alloys, Mater. Sci. Eng., A 773 (2020) 138873.
[112] T.N. Vu, V.T. Pham, T.H. Fang, Influences of grain size, temperature, and strain rate on mechanical properties of Al0. 3CoCrFeNi high–entropy alloys, Mater. Sci. Eng., A 858 (2022) 144158.
[113] Y. Hu, S. Ding, J. Xu, Y. Zhang, W. Wu, R. Xia, Anisotropic orientation dependent shock wave responses of monocrystalline molybdenum, J. Mater. Res. Technol. 25 (2023) 285–296.
[114] M.P. Chang, Y.S. Lu, T.H. Fang, Mechanical mechanism and deformation behavior of polycrystalline and gradient Ni50− xTi50Alx alloys using molecular dynamics, Mater. Today Commun. 28 (2021) 102724.
[115] H.G. Nguyen, T.H. Fang, Machining mechanism and residual stress of AlCuCrFeNi alloy, Int. J. Mech. Sci. (2024) 109429.
[116] A. Eghtesad, Q. Luo, S.L. Shang, R.A. Lebensohn, M. Knezevic, Z.K. Liu, A. M. Beese, Machine learning-enabled identification of micromechanical stress and strain hotspots predicted via dislocation density-based crystal plasticity simulations, Int. J. Plast. 166 (2023) 103646.